A PIV investigation of the effect of disperse phase fraction on the turbulence characteristics of liquid-liquid mixing in a stirred tank

Nannan Liu[a], Wei Wang[ai*1], Jiacheng Han[a], Meng Zhang[a], Panagiota Angeli[b], Changchun Wu[a], Jing Gong[a*]

a. National Engineering Laboratory for Pipeline Safety/Beijing Key Laboratory of Urban Oil & Gas Distribution Technology/ MOE Key Laboratory of Petroleum Engineering, China University of Petroleum, Beijing, China

b. Department of Chemical Engineering, University College London, London, UK. WC1E 7JE

Abstract

In this paper, utilizing 2D angle-resolved particle image velocimetry (PIV), the flow field of a dilute aqueous-in-oil dispersion is experimentally studied in a stirring tank. Opacity during liquid-liquid mixing is eliminated by matching the refractive indices of both phases. Anisotropy of the turbulence flow field is analysed via the turbulent kinetic energy (TKE) and energy dissipation rate (EDR) obtained at different measuring angles. The influence of spatial resolution is compared and discussed. TKE and EDR are observed to increase with increment of dispersed phase fraction while a small range of disorder and fluctuation is observed in the impeller region. The effect of dispersed droplets should be attributed to the strengthened fluctuation of velocities and spatial differences. Further work concerning higher resolution and the disperse fraction is necessary.

Keywords: Liquid-liquid mixing, Turbulence characteristics, Angle-resolved particle image velocimetry, Dispersed phase fraction

1. Introduction

Processes involving disperse immiscible fluids occur in such industries as the food, biochemical, pharmacy, petroleum, chemical, new energy, and mining industries. These processes include emulsification, two-phase reactions, bioprocesses, and liquid-liquid extraction, generating such products as bulk and fine chemicals, pharmaceuticals, nano-particles of various materials and foods. Research on turbulent flow characteristics in multiphase processes are critical for understanding the above operations. Extensive research has been conducted to link quantitative flow parameters to turbulent characteristics in both single phase and multiphase mixing process. Such parameters as turbulent kinetic energy (TKE) and energy dissipation rate (EDR) are widely used. These parameters characterize

1E-mail address:
w.wang@cup.edu.cn(W.Wang),p.angeli@ucl.ac.uk(P.Angeli),ydgj@cup.edu.cn (J.Gong).

the degree of velocity fluctuation over time in fixed areas, as well as spatial and temporal energy consumption (Kresta, 1998; Khan, 2005; Gabriele et al., 2009, 2011; Li et al., 2011).

In a stirred system, the turbulent flow characteristics are extremely complex because the system is non-uniform and anisotropic. The mean dissipation rate, which can be determined from impeller power number or torque measurements, can hardly describe local energy transport (Kresta and Wood, 1993a, 1993b; Zhou and Kresta, 1996; Sharp et al., 1998; Sheng et al., 2000; Delafosse et al., 2011). The methodology for describing EDR distributions based on quantitative velocity fields and the method for evaluating TKE is important.

To acquire information regarding complex velocities in stirred vessels, various experimental techniques, including hot-film anemometry, and optical diagnostic techniques, such as laser-doppler anemometry (LDA), laser-induced fluorescence (LIF) and particle image velocimetry (PIV), are employed (Zhou and Kresta,1996; Jaworski et al., 2001; Khan, 2005; Morgan et al., 2012, 2013). Recently, PIV has become a major contributor to many advances in the understanding of turbulent and complex flows (Westerweel et al., 2013). By applying PIV, instantaneous field information for velocities, as well as field information for root mean square (RMS) velocities and small-scale vortices, could be obtained. For single phase measurements, small scale flow structures around a Rushton turbine (Sharp and Adrian, 2001; Li et al., 2011), angle-resolved specific TKE and EDR distributions (Ducci and Yianneskis, 2006; Gabriele et al., 2009; Delafosse et al., 2011), the influence of PIV spatial resolution on EDR values (Piirto et al., 2000; Saarenrinne et al., 2001; Baldi and Yianneskis, 2003) and the modification of isotropic assumptions in stirred tanks (Delafosse et al., 2011) have been successfully studied. For gas/solid-liquid phase measurements, the use of a spectroscope with two cameras (Sathe et al, 2010) and a particle-isolating algorithm (Ashwood et al., 2015) while matching refraction indices is recommended for liquid-liquid systems to prevent the appearance of opacity (Tabib and Schwarz, 2011; Tabib et al., 2012) and to describe the flow motions of both phases in identical images (Liu, 2005; Svensson and Rasmuson, 2006; Hlawitschka and Bart, 2012). It should be noted that PIV cannot resolve all flow fields due to limitations in camera capacity and the scale of the tracer particles.

In the study of liquid-liquid systems, with the exception of successful measurements of oil-water stratified pipe flows (Kumara et al., 2010; Morgan et al., 2012, 2013), non-intrusive measurement of disperse turbulent flow in stirred systems has rarely been established. Several attempts have been made: Liu (2005)

introduced the LIF method for investigating phase inversion in concentrated immiscible organic-aqueous dispersions, where drop breakage, coalescence and secondary dispersion are clearly demonstrated. However, the LIF method is not appropriate for instant velocity measurements (Liu, 2005; Sathe et al, 2010; Hlawitschka and Bart, 2012). Svensson and Rasmuson (2006) investigated the effect of disperse volume fraction on the flow structure of an immiscible liquid-liquid system using PIV, observing and discussing the change of the vortex centre and velocities of the eject zone around a Rushton turbine. However, knowledge of turbulent properties, such as TKE and EDR, at various disperse volume fractions is particularly lacking.

Research on the effect of disperse phase on turbulence characteristics has primarily focused on gas-liquid and liquid-solid two-phase flows. By applying hot-film anemometry, Iskandrani and Kojasoy (2001) found that turbulence intensity is affected by local void fraction distribution, where the turbulence intensity is slightly suppressed at low void fraction but strongly enhanced at high void fraction. The effect of disperse bubbles during noticeable turbulence enhancement was observed by Sun et al. (2004), who utilized LDA to measure the axial liquid velocity and its fluctuations in air-water flows. Similar results were also obtained by Fujiwara et al. (2004) and Hosokawa and Tomiyama (2004). Gabriele et al. (2011) investigated the influence of particle concentrations on turbulent kinetic energy and energy dissipation rate of a continuous liquid phase using PIV. The results demonstrated that TKE decreases by up to 40%, and EDR decreases by 50%, adjacent to the up-pumping impeller when particle concentration is increase from 0% to 5%. This trend is in accordance with results reported by Unadkat et al. (2009), who observed that addition of solid particles could suppress the maximum energy dissipation rate without affecting the mean flow. Hu (2006) conducted turbulence velocity measurements in both oil and water continuous dispersions using hot-film anemometry. The results showed that turbulence in both dispersions generally increases with increasing input oil fraction. However, turbulence suppression is not as obvious as suggested by the high mixing velocities.

Augmentation or attenuation of turbulence is determined by physical properties, the concentration of the disperse phase, and drop/particle size. Large drops are likely to enhance turbulence intensity, while small drops tend to suppress the fluctuation of the continuous phase. (Iskandrani and Kojasoy, 2001; Fujiwara et al.,2004; Hosokawa and Tomiyama, 2004; Sun et al., 2004; Unadkat et al. 2009; Gabriele et al., 2011). Gabriele et al. (2011) analysed the effect of the disperse

phase in relation to the particle Stokes number (ratio of the fluid dynamic relaxation time of particle to the Kolmogorov timescale). Because small particles' response speeds are higher than the velocity fluctuations, these particles (whose Stokes number is less than 1.0) extract energy from turbulence, leading to turbulence suppression. Large particles, on the other hand, result in turbulence augmentation. Gore and Crowe (1989) concluded that turbulence intensity is augmented when the ratio of particle size to the integral length scale of turbulence exceeds 0.1 and that values below 1.0 result in suppression. Hetsroni (1989) defined the particle Reynolds number ($Re=\rho_p u_r d_p/\mu_c$, where u_r is the relative velocity between the particle and the continuous phase and μ_c is the viscosity of the carrier fluid) and stated that Reynolds numbers above 400 would attenuate turbulence. Using a hybrid turbulence length scale, Kenning and Crowe (1997) derived an equation that determines changes in turbulence intensity by balancing the production of inherent turbulence, production due to disperse phase, loss of turbulence energy from viscous dissipation and the retransmission of energy to solid particles.

In summary, research on the effect of a disperse phase on turbulence flow in liquid-liquid disperse systems is still lacking. The present study aims to determine the effect of disperse fraction experimentally. The oil-water two-phase instantaneous velocity fields at various disperse fractions (dilute dispersion) are measured using 2D-PIV by matching the refractive indices of two phases. The influence of spatial resolution and angle-resolved plane are discussed. Based on an isotropic assumption, TKE and local EDR distributions are determined by calculating velocity gradients and comparing the gradients at various disperse fractions.

2. Materials and Methods

2.1 Configuration and fluid properties

Experiments are conducted in a flat-bottomed borosilicate glass beaker (width T=80 mm, height H=80 mm(400ml)) equipped with a four pitched-blade impeller (diameter D=50 mm (D/T=0.625), width7.5 mm, height 5.0 mm, inclination angle 45°, provided by IKA) as shown in Fig. 1(a). The beaker is surrounded with water in a rectangular tank to minimize errors due to curvature effects from a cylindrical tank and from differences in refractive index between the beaker glass and the experimental liquids. To protect the CCD camera, the impeller is painted black to minimise laser reflections. The total volume of the liquid-liquid mixture is maintained at 400 ml, and the dispersed (aqueous phase) volume fraction is set to

0%, 0.2%, 0.5%, 0.7%, 1.0% and 1.3%. In the presence of a secondary liquid phase, a fully disperse system generally presents as oyster white, hindering the flow visualization of both phases. To gain clear data from the laser induced plane, the aqueous phase is a solution of 80% glycerol in 20% deionized water by weight to match the refractive index of oil phase (Exxsol D130 oil). The physical properties of the experimental fluids are shown in Table.1. During the experiment, the aqueous phase, which has a higher density and viscosity, is retained as the disperse phase. The impeller is placed 6 mm above the bottom, and its rotation speeds is maintained at 700 rpm, providing a Reynolds number $Re=\rho ND^2/\mu_c$(4807) (where μ_c is the viscosity of continuous phase, N is the rotation speed and D is diameter of impeller) when fully dispersed.

2.2 PIV system and image processing

As shown in Fig.1(b), the 2D-PIV system consists of a Nd-YAG dual pulse laser (emission wave length 532 nm), a FlowSense EO 40 CCD camera equipped with a Nikon lens (AF Micro Nikon 60 mm F2.8D) capable of capturing 15 image pairs per second with a resolution of 2048×2048 pixels^2, a timerbox to synchronize the image capture with the laser pulses (Dantec Dynamics 80N77) and Dynamic Studio software. The seeding particles used are Polyamide Seeding Particles (5μm diameter, density 1.03 g/cm^3) provided by Dantec with a sufficiently small relaxation time to follow the motion of fluid. During the image acquisition process and in agreement with previous researchers (Chung et al., 2009; Delafosse et al., 2011; Gabriele et al., 2009, 2011), the laser-induced plane is chosen to be the vertical plane along the height of the vessel. Only half of the plane is focused due to symmetry (Fig. 1(a)). A shaft encoder connected to a timerbox is employed to control the impeller position when measuring the plane. In the present work, due to the symmetry of pitched-blade impeller, the angle between the impeller blade and the measuring plane is set to 0°, 22.5°, 45° and 67.5° to demonstrate the anisotropy of flow in the stirred tank. For each experiment, 100 pairs of images are recorded for velocity calculations. In each pair of images captured, the time between pluses, which depends on impeller rotation speed, is kept at 100 μs for various disperse phase fractions to record fluid motion near the impeller exactly. Images are handled by Dantec Software to remove background.

For each pair of images handled, velocity vectors are computed in three steps: First, the adaptive-correlation technique is used, including a final interrogation area (IA) setup. Overlap values are chosen to produce the coarse velocity vector map. Secondly, large error vectors are eliminated using UV Scatter plot Range

Validation and Moving average validation. Finally, an average filter over 3×3 pixels^2 is performed to produce a smooth flow velocity vector map. The resolution of the PIV is limited by the scale of the individual interrogation area (Δ), as eddy characteristic lengths smaller than Δ can hardly be resolved due to the relatively low magnification. To obtain the intensities of the tracer particles, two different areas (32×32, 16×16 pixels^2) are used to investigate the influence of spatial resolution on estimated turbulent flow field (Piirto et al., 2000; Saarenrinne et al., 2001; Baldi and Yianneskis, 2003).

3. Turbulent Flow Properties

PIV yields basic velocity distributions in the measuring plane. To determine turbulent properties such as TKE and EDR, the velocity data must be processed further. In this section, the determination of TKE using an isotropic assumption and EDR using various estimation methods are described. Besides, averaging of both TKE and EDR on specific flow range is depicted.

3.1 Estimation of turbulent kinetic energy

Characterized by instantaneous fluctuations of velocity U in full range flow, the velocity of a turbulent flow is generally split into an ensemble-averaged mean component $\bar{u}$ and a fluctuating component u', which can be expressed as

$$U = \bar{u} + u' \tag{1}$$

The degree of deviation from the mean velocity is represented as a root mean square (RMS), as values of the fluctuating component u' may be negative or positive:

$$\bar{\bar{u}} = \sqrt{\overline{u'^2}} = \sqrt{\overline{\left(U - \bar{u}\right)^2}} \tag{2}$$

The velocity contains a periodic fluctuation component and a temporal velocity in the impeller driven system, which can be decomposed into

$$U = \bar{u}_\theta + u'' \tag{3}$$

$$U = \bar{u} + u_p + u'' \tag{4}$$

Where $\bar{u}_\theta$ represents the angle-resolved mean velocity, u'' represents pure velocity fluctuations due to turbulence and u_p represents periodic velocity fluctuations due to blade passage.

For the Cartesian coordinate system, turbulent kinetic energy is determined by the three velocity components and is expressed as

$$k = \frac{1}{2}\left(\bar{\bar{u}}^2 + \bar{\bar{v}}^2 + \bar{\bar{w}}^2\right) \tag{5}$$

In Eq.5, the third fluctuating velocity component cannot readily be obtained from 2D PIV. Khan (2005) considered $\overline{w}^2 = \overline{u}^2$ and the form of TKE was taken as

$$k = \frac{1}{2}\left(2\overline{u}^2 + \overline{v}^2\right) \tag{6}$$

In addition, the $\overline{w}^2$ component can be characterized by a combination of $\overline{u}^2$ and $\overline{v}^2$ (Gabriele et al.,2009):

$$\overline{w}^2 = \frac{1}{2}\left(\overline{u}^2 + \overline{v}^2\right) \tag{7}$$

Consequently, TKE can be estimated from

$$k = \frac{3}{4}\left(\overline{u}^2 + \overline{v}^2\right) \tag{8}$$

Adopting an angle-averaged RMS $\overline{u} = \sqrt{\overline{u''^2}}$ is more representative, and this angle-averaged RMS has been used to estimate the local energy dissipation rate to investigate anisotropy in the turbulent flow field (Gabriele et al., 2009). In the current work, Eq.8 is used because an angle-resolved measurement indicates that radial velocity distributions are affected by the position of the impeller.

3.2 Direct estimation of energy dissipation rate (DE)

The turbulent energy dissipation rate can be estimated from its definition, which is comprised of a viscosity term and the derivative of the RMS gradient. The predicted viscosity applied in the experimental analysis is based on Brinkman (1952). The tensor expression of the energy dissipation rate (ε) is shown in the following (Hinze,1959):

$$\varepsilon = \nu\overline{\left(\frac{\partial u_i}{\partial x_j} + \frac{\partial u_j}{\partial x_i}\right)\frac{\partial u_j}{\partial x_i}} \tag{9}$$

Expanding the tensor form in the Cartesian coordinate system, the local energy dissipation rate can be calculated from

$$\varepsilon_{DE} = \nu\left\{\begin{array}{l} 2\overline{\left(\frac{\partial u'}{\partial x}\right)^2} + 2\overline{\left(\frac{\partial v'}{\partial y}\right)^2} + 2\overline{\left(\frac{\partial w'}{\partial z}\right)^2} + \overline{\left(\frac{\partial u'}{\partial z}\right)^2} + \overline{\left(\frac{\partial v'}{\partial x}\right)^2} \\ + \overline{\left(\frac{\partial u'}{\partial y}\right)^2} + \overline{\left(\frac{\partial w'}{\partial x}\right)^2} + \overline{\left(\frac{\partial v'}{\partial z}\right)^2} + \overline{\left(\frac{\partial w'}{\partial y}\right)^2} \\ +2\left(\overline{\frac{\partial u'}{\partial y}\frac{\partial v'}{\partial x}} + \overline{\frac{\partial u'}{\partial z}\frac{\partial w'}{\partial x}} + \overline{\frac{\partial v'}{\partial z}\frac{\partial w'}{\partial y}}\right) \end{array}\right\} \tag{10}$$

The subscript *DE* indicates that the energy dissipation is calculated from a direct

evaluation adopted by Gabriele et al. (2009). The isotropy assumption in 2D PIV system is employed to simplify Eq.10 (Sharp and Adrian, 2001; Khan, 2005; Gabriele et al., 2009; Delafosse et al., 2011), which is taken as

$$\varepsilon_{DE}=\nu\left\{2\overline{\left(\frac{\partial u'}{\partial x}\right)^2}+2\overline{\left(\frac{\partial v'}{\partial y}\right)^2}+3\overline{\left(\frac{\partial u'}{\partial y}\right)^2}+2\overline{\left(\frac{\partial v'}{\partial x}\right)^2}+2\overline{\frac{\partial u'}{\partial y}\frac{\partial v'}{\partial x}}\right\} \quad (11)$$

Referring to the energy cascade theory proposed by Kolmogorov (1941), direct interactions between the large energy-containing eddies and the small energy-dissipating eddies do not exist. Instead, kinetic energy is transferred from large to small eddies in a cascade based on the kinetic energy spectrum of turbulence (Baldyga and Podgorska, 1998). The process of energy transport from large to small-scale eddies is independent of viscous forces, where turbulent kinetic energy is finally transferred to the smallest eddies (Kolmogorov length scale) and is dissipated into heat caused by friction between the fluid molecules due to fluid dynamic viscosity (Gabriele et al., 2011). Therefore, to estimate the EDR, the effect of turbulent eddies down to the Kolmogorov length scale should be considered. Generally, the Kolmogorov length scale is given as

$$\lambda_k=\left(\frac{\nu^3}{\varepsilon}\right)^{1/4} \quad (12)$$

Assuming that EDRs are uniform in the stirred tank, the mean EDR can be estimated from

$$\overline{\varepsilon_T}=\frac{P}{\rho_m V} \quad (13)$$

Where V is the volume of the fluid, P is the power calculated from $P=P_o\rho_m N^3 D^5$, and P_o is the power number, which depends on the type of impeller. For a four pitched-blade impeller, P_o=3.0 (Tsouris and Tavlarides, 1994). In this work, the mean Kolmogorov length (λ_k) is 50 μm, calculated based on the continuous viscosity and the mean EDR ($\overline{\varepsilon_T}=3.72 m^2 s^{-3}$). The spatial resolutions of the measurements(Δ)are 630 μm (32×32 pixels^2) and 315 μm (16×16 pixels^2) and Δ/λ_k is 12.6 and 6.3, respectively.

Saarenrinne et al. (2001) stated that EDRs estimated from direct measurements are difficult to sufficiently resolve, with 90% EDR resolution requiring Δ/λ_k=2.0 and 65% EDR resolution requiring Δ/λ_k=9.0.

3.3 Modified estimation of energy dissipation rate

As stated above, direct PIV experimental data are unable to resolve the smallest length scale, resulting in underestimation of turbulent dissipation (Hlawitschka

and Bart, 2012). Several modified estimation methods are performed.

3.3.1 Modified direct estimation (MDE)

A correction factor f_e for modification of PIV resolution is described by Hlawitschka and Bart (2012) as:

$$f_e = 1 - \exp\left(-\frac{3}{2}\alpha\left(\frac{\pi}{\Delta}\eta\right)^{4/3}\right) \tag{14}$$

$$\eta = \left(\nu^3 f_e / \varepsilon\right) \tag{15}$$

$$\varepsilon_{MDE} = \varepsilon_{DE} / f_e \tag{16}$$

Where α is a constant equal to 1.6, and ε_{MDE} is computed iteratively as follows: in the first circle, f_e is taken as unity, and the value of η is estimated from the hypothetical value of ε, where $\varepsilon=max(\varepsilon_{MDE})$ (Hlawitschka and Bart, 2012). In the second cycle, f_e is calculated from Eq.14, and η is recalculated.

3.3.2 Large Eddy Simulation (SGS-LES)

Another means of modifying the EDR estimation for relatively low spatial resolutions is the Large Eddy Simulation (LES) proposed by Sheng et al. (2000). As described in Section 3.2, turbulence energy is generated at large scales and dissipated in the viscous sub-range. Eddy scales are below the Kolmogorov length scale. In the inertial sub-range, where the eddy scale varies from large scale to the Kolmogorov length scale, turbulent energy production or dissipation does not occur. Instead, turbulent kinetic energy transfer from large eddy to small eddy occurs only by the kinetic energy spectrum of turbulence. The quantities of TKE transferred in the inertial sub-range are the same as the energy dissipated in the viscous sub-range. Therefore, it is unnecessary to estimate the energy dissipation down to the Kolmogorov length scale. Instead, it is necessary to compute the TKE transferred in the inertial sub-range.

The LES method is adapted to resolve the filtered Navier-Stokes (NS) equations for the large resolved scales. The filtered small scales are characterized by the sub-grid-scale (SGS) turbulence model. If the filtering scales are within the inertial sub-range according to Sheng et al. (2000) and Klan (2005), the turbulence dissipation rate can be estimated by the SGS energy flux at the cut off scale (filter width) that corresponds to the PIV resolution based on a local isotropy assumption. In the current study, the spatial resolution scales (filtering scales) are 630 μm and 315 μm and are smaller than the integral length scale (D/10=5 000μm, Kresta and Wood, 1993a). The mean Kolmogorov length scale is calculated to be 50 μm, and this length scale is expected to lie within the inertial sub-range. Therefore, the

energy dissipation can be estimated from

$$\varepsilon \approx \varepsilon_{SGS} = -2\overline{\tau_{ij} s_{ij}^{'}} \tag{17}$$

Where $s_{ij}^{'}$ is the strain rate tensor that can be calculated from the measured velocity field $s_{ij}^{'} = 1/2\left(\partial u'_j/\partial x_i + \partial u'_i/\partial x_j\right)$, τ_{ij} is SGS stress tensor. The eddy viscosity model (Smagorisky, 1963) is adopted for the closure of SGS stress, which is taken as

$$\tau_{ij} = -C_s^2 \Delta^2 \left|s'_{ij}\right| s'_{ij} \tag{18}$$

Where C_s is the Smagorinsky constant (C_s =0.13 is used in this work) (Gabriele et al., 2009), Δ is the filter width, which indicates the length of interrogation window, and $C_s^2\Delta^2\left|s'_{ij}\right|$ indicates the eddy viscosity. $\left|s'_{ij}\right|$ is taken as $\left|s_{ij}^{'}\right| \approx \sqrt{2s_{ij}^{'}s_{ij}^{'}}$. Hence:

$$\varepsilon_{SGS} = -C_s^2 \Delta^2 \left(2s'_{ij}\, s'_{ij}\right)^{3/2} \tag{19}$$

By compensating for the third unknown velocity component based on the isotropic assumption, ε_{SGS} can be estimated from velocity field determined via 2D-PIV (Khan, 2005).

$$\varepsilon_{SGS} = C_s^2 \Delta^2 \left\{ 4\overline{\left(\frac{\partial u'}{\partial x}\right)^2} + 2\overline{\left(\frac{\partial v'}{\partial x}\right)^2} + 2\overline{\left(\frac{\partial u'}{\partial y}\right)^2} + 4\overline{\left(\frac{\partial v'}{\partial y}\right)^2} \right\}^{3/2} \tag{20}$$

3.3.3 Dimensional analysis (DA)

Based on the fact that most energy enters turbulent flow in the form of large-scale motion and is contained in large eddies, as well as the fact that flow is in local equilibrium, Kresta (1998) suggested dimensional analysis (the DA method) for EDR estimation. The expression of the method has two forms:

$$\varepsilon = A\frac{u_{rms}^{'3}}{L} \tag{21}$$

$$\varepsilon = A\frac{k^{3/2}}{L} \tag{22}$$

In Eq.21, A is a constant equal to 1.0 and L is the integral length scale. In Eq.22, k is the value of TKE and A=0.8. Kresta and Wood (1993b) stated that the calculations of both methods are nearly equivalent. Various values of the integral length scale L have been proposed: D/5.5 or 7.2 (Laufhutte and Mersmann, 1985); D/6.0 (Costes and Couderc, 1988); D/12.5 (Wu and Patterson, 1989) and D/10.0 (Kresta and Wood, 1993a). In this paper, the integral length scale L=D/7.2 is used.

3.4 Averaging of estimated TKE and EDR

To reflect the turbulence characteristics, mean distribution of TKE and EDR

between four measuring angles are calculated as:

$$\overline{\psi} = \frac{1}{4}\sum_{i=1}^{4}\psi_i \tag{23}$$

Where ψ_i is either k or ε at each angles while $\overline{\psi}$ is the mean value.

To demonstrate the un-homogeneity of turbulence in the stirred tank, the whole measuring plane is divided into two areas: the impeller region with position of 0<H<15.75mm and 0<T<36mm (light blue colour area in Fig.1 (a)), and the circulation region occupying the location 15.75<H<80.0mm and 0<T<36mm (dark blue colour area in Fig.1 (a)). To quantitatively analyse the effect of different factors on turbulence, both mean values of TKE and EDR in the impeller region, circulation region and full region are calculated respectively by integrating values at each grid and then averaging to the region, and general expression is taken as:

$$\overline{\Gamma} = \frac{\sum_{i=R_{ll}}^{R_{ul}}\sum_{j=H_{ll}}^{H_{ul}}\Gamma_{i,j}}{\left(R_{ul}\text{-}R_{ll}+1\right)\times\left(H_{ul}\text{-}H_{ll}+1\right)} \tag{24}$$

Where $\Gamma_{i,j}$ is the specific mean value of either angle averaged TKE ($\overline{k}$) or EDR ($\overline{\varepsilon}$) at each grid while $\overline{\Gamma}$ is the mean value on the fixed region either $\overline{\overline{k}}$ or $\overline{\overline{\varepsilon}}$; R_{ll} and H_{ll} are the lower limit in the X and Y axils, R_{ul}, H_{ul} are the upper limit. Parameters above are agree with division of region as indicated in Fig.1 (a).

4. Results and Discussion

In this section, the effect of disperse phase fraction on TKE and EDR are discussed and analysed in Sec.4.1. The influence of spatial resolution on the resolved TKE and EDR at different disperse phase fraction is discussed in Sec.4.2. TKE and EDR distributions at various measuring angles are shown in Sec.4.3. Effects of the estimated method on EDR is considered in Sec.4.4.

4.1 Effects of disperse phase fraction on TKE and EDR

Since the values of TKE and EDR vary with measuring angle, results of 0°, 45°and the mean value are presented for discussion.

4.1.1 Effects of disperse phase fraction on TKE

Angle-resolved TKE distribution at 0°at different dispersed fractions is shown in Fig. 2. Comparing Fig. 2 (a) to (f), in the impeller region, the vortex area (red colour) representing the highest TKE increases from 0 to 0.2%, then decreases

364 from 0.2% to 1.0%, and increases above 1.0%. In the circulation region, the TKE
365 monotonically increases with the addition of the dispersed phase, where the TKE
366 first increases near the impeller shaft and top edge of the tank, and later expands
367 from the top to the middle part of tank. However, in the TKE distribution at 45°
368 (Fig. 3) the vortex area in the impeller discharge region increases from 0% to 0.7%,
369 decreases in 1.0%, and later increases above 1.0%. Fig. 4 shows the mean TKE
370 distribution in which changes of TKE in the impeller region are slightly fluctuated
371 but an increasing trend is shown in the circulation region with increase of the
372 dispersed fraction.
373 In accordance with the contour map in Fig.2 to 4, angle averaged mean TKE
374 values of different dispersed fraction in impeller region, circulation region and full
375 region are shown in Table.2. It's clear that the mean TKE of pure oil system in
376 impeller region is lower than that in the dispersion, while with the increment of
377 dispersed phase, there is a small discrepancy, where those at 0.2% to 0.7% is 1.11
378 times as the pure, and 1.07 and 1.25 times for 1% and 1.3%. However, mean TKE
379 in circulation region increases with addition of dispersed phase, varying from 1.10
380 times at 0.2% to the 2.29 times for 1.3% dispersion. Deviation of TKE between the
381 impeller and circulation region eliminates with disperse fraction increment,
382 where the mean TKE of pure system in impeller region is 5.74 times
383 (=0.0178/0.0031) of the circulation region and 3.14 times (=0.0223/0.0071) at
384 1.3% dispersion. It indicates the role of dispersed phase on the turbulence
385 homogenizing. For the mean TKE in full region, a monotonous increasing trend is
386 found and it's 1.76 times as the pure system in 1.3% dispersion system.
387 Generally, for single phase mixing, TKE and velocity fluctuations would be
388 inhibited at higher density and viscosity. In the dilute aqueous solution (glycerol
389 and water) in oil dispersed system, both density and viscosity of the mixture
390 increase slightly with increasing dispersed fraction, which may contribute to the
391 inhibition of TKE in the impeller region shown in Fig. 2 (b) to (e) and Fig. 3 (d) to
392 (e). The existence of dispersed droplets enhances the transfer of momentum and
393 energy from regions of high turbulent intensity (Hu, 2006) including transfer from
394 region close to impeller blade to the discharged region and from impeller region
395 to the circulation region. Increased number of droplets with disperse fraction
396 could transfer more kinetic energy from impeller, resulting in an increment of TKE
397 in impeller region as shown in Fig.2(a) to (b), Fig.3(a) to (d) and in the circulation
398 region in Fig. 2-4.
399 In addition to the influence of droplet number, the droplet size could also affect
400 the TKE. Based on literature on liquid-liquid stirring systems (Tsouris and

401 Tavlarides, 1994; Podgórska, 2009; Maaß, 2010,2012; Wang et al., 2014), drop size
402 in the impeller region is smaller than in circulation region, where large drops and
403 bubbles are likely to augment turbulence intensity, while smaller ones tend to
404 suppress the fluctuation of a continuous phase (Iskandrani and Kojasoy, 2001;
405 Fujiwara et al., 2004; Hosokawa and Tomiyama, 2004; Sun et al., 2004; Unadkat et
406 al., 2009; Gabriele et al., 2011). As the dispersed fraction increases, augmentation
407 of TKE in the middle and top parts of the tank is also attributed to the increase in
408 the number of larger droplets (Fig. 2-4), while in the impeller region, the number
409 of smaller drops increase resulting in the local suppression of turbulence intensity,
410 as seen in Fig. 2 (b) to (e) and Fig. 3 (d) to (e). With further increment of dispersed
411 fraction, drop coalescence is supposed to occur even in the impeller region,
412 resulting in birth of larger droplets, augmenting the TKE, reflected in Fig.2-(e) to
413 (f) and Fig.3-(e) to (f).
414 It is also determined that the decrease in vortex area near the impeller is slightly
415 different between Fig. 2 and 3, where the decrease persists from 0.2% to 1.0% (0°)
416 in contrast to from 0.7% to 1.0% (45°). This difference could be because the
417 inertial force causing droplet breakage at angle 0° is stronger than at 45°, resulting
418 in larger numbers of small droplets which further suppress the turbulence
419 intensity. Though there are TKE variations at different angles due to anisotropy,
420 mean TKE increases with increases in dispersed fraction (Fig. 4).

421 **4.1.2 Effects of disperse phase fraction on EDR**

422 EDR distribution (0°) with DE method at various dispersed fraction is shown in
423 Fig. 5. In the impeller region, the area of maximum EDR (red colour) increases with
424 dispersed fraction up to 0.7% (Fig. 5 (a) to (d)) and slightly decreases at 1.0% and
425 increases again at 1.3% (Fig. 5 (f)). The EDR monotonically increases in the
426 circulation region. Similar trends are observed at 45° (Fig. 6). However, the
427 observed EDR in impeller region fluctuates at various resolved angles and
428 disperse fractions, while the mean EDR distribution hasn't shown obvious
429 variation. Instead, the mean EDR distribution increases with dispersed fraction
430 (Fig. 7). Table.3 shows the angle averaged mean EDR values in impeller region,
431 circulation region and full region, respectively. Similar trend as TKE in Table.2 is
432 found in Table.3. The increment on EDR is found to be larger compared to TKE,
433 where average mean EDR (0.2% to 1.3% total average) in impeller region is 1.30
434 times as the pure while average TKE is 1.13 times. In circulation and full region,
435 EDR is 3.15 and 2.04 times while TKE is 1.61 and 1.37 times.
436 Based on its definition (Eq.9), EDR is influenced by kinematic viscosity, density

and the derivative of the RMS fluctuating velocity gradient with respect to spatial location. As the aqueous dispersed fraction increases mixture viscosity increases and tends to enhance the energy dissipation; meanwhile, it also inhibits the RMS gradient of fluctuating velocities and could lead to a decrease in the EDR. Areas of higher EDR in the impeller region increase with dispersed fraction in Fig. 5 (a) to (d) (0-0.7%) and Fig. 6 (a) to (b) (0-0.2%) and (d) to (e) (0.7%-1.0%), which could be due to its positive effects, otherwise a negative effect on the RMS gradient is dominant in Fig. 5 (d) to (e) (0.7%-1.0%) and Fig. 6 (b) to (d) (0.2%-0.7%).

The influence of the dispersed fraction on EDR is also related to the droplet behaviour, where the breakup and coalescence of droplets could potentially accelerate the EDR (Hu, 2006). The occurrence of drop coalescence increases with the dispersed fraction, which results in the enhancement of the EDR in the circulation region. Additionally, increased drop number and deformed drop shape due to inertia (continuous phase) or drop collision may also strengthen the fluctuation of velocities and their spatial differences, which could be reasonable that the increment on EDR is larger compared to TKE as indicated in Table.2 and Table.3.

4.2 Influence of the spatial resolution on TKE and EDR

Several previous works (Saarenrinne et al, 2001; Baldi and Yianneskis, 2003; Delafosse et al., 2011) indicate that values of the turbulent properties including the TKE and EDR estimated by PIV are strongly influenced by the spatial resolution. Delafosse et al. (2011) concluded that the spatial resolution should be of the same order of magnitude as the Kolmogorov scale (e.g., Δ/λ_k=1.0) to provide an accurate estimation of the EDR. Different from previous research on single phase mixing (Saarenrinne et al., 2001; Delafosse et al., 2011), the influence of spatial resolution on the estimated TKE and EDR is investigated using spatial resolutions of 32×32 pixels^2 (Δ/λ_k=12.6) and 16×16 pixels^2 (Δ/λ_k=6.3) to obtain a full range of turbulence fields in both the single and two-phase dispersion systems.

Fig. 8(a) presents a comparison of the mean TKE distribution (average of four angle-resolved values) in a single oil phase for different two spatial resolutions. Although both resolutions show similar trends, the TKE obtained using the high resolution (16×16 pixels^2) is larger. In contrast to large IA, which tends to omit turbulent fluctuations of small velocities brought by small eddies, small IA would reserve higher numbers of local velocities and smaller turbulent eddies. Increased numbers of resolved velocity vectors are more likely to enhance the TKE. Comparison of the TKE distribution in the 0.5% dispersed system for the two

spatial resolutions is shown in Fig. 8(b). Similar trends as in Fig. 8(a) are found; however, the TKE in the 0.5% dispersed system has a more apparent increase than in the pure system. Comparison of angle averaged mean TKE at the full region is presented in Table.4. Increment Δ_k is introduced to characterize the variation due to spatial resolution changes, calculated as $\Delta_k = \left(\overline{\overline{k_{16}}} - \overline{\overline{k_{32}}}\right) \Big/ \overline{\overline{k_{32}}} \times 100\%$. It can be gained that dispersed phase magnify the deviation of TKE between two resolutions, where increment at pure system is 81%, 166% in 0.5% and 249% for 1.0% dispersion. It is attributed to the enhanced local turbulent intensity, because small IA has the capacity to resolve motions of a larger number of droplets and velocity fluctuations.

Comparison of the mean turbulent EDR distribution (DE method) between different spatial resolutions is provided in Fig. 9. With a spatial resolution of 16×16 pixels^2 the values of EDR increase and the regions with these high values are larger, which indicates an enhanced RMS velocity fluctuation. Due to the randomness of turbulence and flow anisotropy in a stirred tank, the gradient of RMS velocity with respect to spatial location may have a larger discrepancy for small IA.

Comparing to the single oil system, the liquid-liquid dispersion shows a higher EDR, while the effect of spatial resolution is more obvious, depicted by Δ_ε ($\Delta_\varepsilon = \left(\overline{\overline{\varepsilon_{16}}} - \overline{\overline{\varepsilon_{32}}}\right) \Big/ \overline{\overline{\varepsilon_{32}}} \times 100\%$) in Table.5 ($\Delta_\varepsilon$ =1075% in pure system, 1793% and 2409% in 0.5% and 1.0% dispersion). It's attributed to the influence of droplets on the turbulent flow field, where higher spatial resolution could further resolve the effect of deformed interfaces and droplet interactions on the energy dissipation rate. It is important that the influence of spatial resolution on EDR is evident larger than on TKE (Table 4 and 5).

4.3 Effects of measuring angle on TKE and EDR

Fig.10 to 12 shows the angle-resolved TKE distribution as a function of measuring angle related to the impeller blade in a pure oil phase, 0.5% and 1.0% dispersion with an IA of 32×32 pixels^2, respectively. As shown in Fig.10 to 12, with the impeller circulating perpendicular to the measuring plane, the TKE values in both impeller and circulation region decrease with increasing measuring angle, as TKE values at 45°and 67.5° are obviously smaller than the values at 0°and 22.5°. Deviations in impeller regions are because the vortex with a large TKE value generated by the impeller tip moves away from the blade and diffuses in bulk flow.

Diversity in the circulation region can be attributed to intensity discrepancies in the periodic fluctuations in the impeller rotating circle. The fixed wall boundary also enhances irregular velocity fluctuations.

The angle-resolved EDR estimated with the DE method is shown in Fig. 13 to 15. In accordance with the TKE distributions in Fig.10 to 12, energy is primarily dissipated in the impeller region and in areas close to the wall boundary. The differences in TKE and EDR at different angles indicate the anisotropy of turbulent flow in the stirred system. It is clear that TKE is consistent with EDR transfer, either when tip vortices drift across the impeller region or when periodic and fluctuating turbulent flow occurs in the circulation region, suggesting the instantaneous coexistence of generation, transportation and dissipation of energy in turbulent flow.

To investigate the effect of disperse fraction on the deviation of TKE and EDR at different measuring angles, coefficient of variation (V_k) is employed.

TKE
$$V_k = \frac{\sigma_k}{\bar{\bar{k}}} \times 100\% \tag{25}$$

$$\sigma_k = \sqrt{\frac{\sum_{i=1}^{4} (\bar{k}_i - \bar{\bar{k}})^2}{4}} \tag{26}$$

Where, V_k is the coefficient of variation and σ_k is the standard deviation. Similarly, coefficient of variation of EDR is given as

EDR
$$V_\varepsilon = \frac{\sigma_\varepsilon}{\bar{\bar{\varepsilon}}} \times 100\% \tag{27}$$

Table 6 and 7 present the effect of disperse fraction on the TKE and EDR of full region at different measuring angles. Results further prove the trend depicted in Fig.10 to12 and 13 to15. Besides, both coefficients of variation of TKE and EDR are found to first increase (pure to 0.2% dispersion) then decrease (0.2%-1.3% dispersion). It is proposed that homogenizing effect caused by mass and momentum transfer gradually dominates with the dispersed fraction increases.

4.4 Influence of estimated method on EDR

Fig. 16 shows a comparison of the mean EDR with 32×32 pixels^2 from a single oil phase using different estimation methods, including the direct evaluation method (DE), the SGS model applied in Large Eddy Simulation (LES), the modified direct evaluation method (MDE) and dimensional analysis (DA). It is clear that the EDR distribution obtained from these four methods shows a similar trend that high EDR is primarily in the impeller region. MDE represents a larger distribution

(red area) than DE while DA is larger than DE only in the impeller region. Distribution of EDR estimated from LES is the smallest. Similar findings are obtained from the dispersed system where the EDR distribution in 0.5% and 1.0% dispersed system are provided in Fig. 17 and Fig.18.

Table.8 to 10 describes the angle averaged mean EDR using different methods at full, impeller and circulation region. Calculated EDR using LES method is nearly 0.51 times as the EDR using DE method, while 1.68 times and 1.37 times using the MDE and DA method. Different from the full region, the EDR increment calculated using LES and DA method is higher in impeller region comparing with DE method (LES is 0.71 times to DE and DA is 1.89 times to DE). However, the above increment diminishes in circulation region, e.g. EDR using DA is 0.93 time to DE. Besides, the effect of disperse fraction on the deviation of calculated EDR using different methods is still not clear.

Methods LES, DA and MDE are supposed to have the ability to overcome the limitation of spatial resolution of the 2D-PIV system. Hlawitschka and Bart (2012) indicated that values estimated from LES, DA and MDE are larger than those from DE in a single water system. In the current work, EDR using LES in full region and using DA in circulation region is smaller than DE, which is attributed to the continuous phase is oil phase with higher viscosity, but its influence is only reflected in DE method. Further, the integral length scale considered in DA and the Smagorinsky constant in LES might be the possible explanation for the deviation.

Recently, experimental findings have demonstrated that turbulence in liquid-liquid dispersions is more complicated than in particle–liquid dispersions (Hetsroni, 1989), which is in contrast to particle-liquid systems, where scale and concentration of particles are determined and the number, sizes and distribution of droplets are influenced by the dispersed phase fraction and turbulence intensity in the liquid-liquid system. Drop deformation brings difficulties to clarify its effect of augmentation or suppression based on mechanism of particle. Because drops continuously break and coalesce, their shapes and interface variations can magnify the error of the refractive index between the continuous and dispersed phase. In a concentrated dispersion, the number of drops increases, and the phase overlap leads to a large error of refractive index. The above conditions could result in two adverse consequences for PIV measurements: the appearance of opacity in the mixing process and distortion of light emitted by the laser generator and reflected by the tracer particles. Therefore, the present work aims to provide experimental knowledge in liquid-liquid dispersion.

5. Conclusions

In this paper, an experiment utilizing angle-resolved PIV on flow field analysis of an aqueous-in-oil dispersion is performed. Opacity during liquid-liquid mixing is eliminated by matching the refractive index of both phases. Turbulent characteristics are expressed by two primary parameters: TKE and EDR. Four methods for local EDR estimation are considered: DE, MDE, DA and LES.

TKE and EDR are found monotonously increase with the increment of the dispersed phase fraction in the circulation region, while a small range of disorder and fluctuation is observed in the impeller region. The effect of mixture viscosity, number and size of droplets and shape changes should be attributed to strengthen the fluctuation of velocities and their spatial differences. The influence of spatial resolution on TKE and EDR suggests that higher resolution results in larger values of TKE and EDR and it is magnified by the increment of disperse fraction. The effect of measuring angle on TKE and EDR is analysed and provides an insight into the anisotropy of the turbulence of both single phase and liquid-liquid dispersion in the stirred tank. Deviation of TKE and EDR between different angles is found to decrease with addition of disperse phase. Besides, TKE transfer is found consistent with EDR routine in the process of tip vortices drifting across the impeller region or periodic and fluctuating turbulent flow in a circulation region. Fully resolved EDR distribution at the Kolmogorov length scale is extremely challenging due to the difficulties in distinguishing the EDR estimation accurately. Further work investigating higher resolution measurements on turbulent flow fields and EDR estimation is necessary.

Acknowledgement

The authors wish to thank the National Natural Science Foundation of China (51422406, 51534007), the Henry Fok Foundation (142021), the Foundation for the Author of National Excellent Doctoral Dissertation of PR China (201254), and Science Foundation of China University of Petroleum Beijing (2462015YQ) for providing support for this work.

Reference

Ashwood, A.C., Vanden Hogen, S.J., Rodarte, M.A., Kopplin, C.R., Rodríguez, D.J., Hurlburt, E.T., Shedd, T.A., 2015. A multiphase, micro-scale PIV measurement technique for liquid film velocity measurements in annular two-phase flow. Int. J. Multiph. Flow 68, 27–39.

Bałdyga, J., Podgorska, W., 1998. Drop break-up in intermittent turbulence: Maximum stable and transient sizes of drops. Can. J. Chem. Eng. 76, 456–470.

Brinkman. H.C., 1952. The viscosity of concentrated suspensions and solutions, J.Chem.Phys. 20, 571-581.

Baldi, S., Yianneskis, M., 2003. On the Direct Measurement of Turbulence Energy Dissipation in Stirred Vessels with PIV. Ind. Eng. Chem. Res. 42, 7006-7016.

Costes, J., Couderc, J.P., 1988. Study by laser Doppler anemometry of the turbulent flow induced by a Rushton turbine in a stirred tank: influence of the size of the units II. Spectral analysis and scales of turbulence. Chem. Eng. Sci.43,2765–2772.

Chung, K.H.K., Simmons, M.J.H., Barigou, M., 2009. Local gas and liquid phase velocity measurement in a miniature stirred vessel using PIV combined with a new image processing algorithm. Exp. Therm. Fluid Sci. 33, 743–753.

Ducci, A., Yianneskis, M., 2006. Turbulence kinetic energy transport processes in the impeller stream of stirred vessels. Chem. Eng. Sci. 61, 2780–2790.

Delafosse, A., Collignon, M.L., Crine, M., Toye, D., 2011. Estimation of the turbulent kinetic energy dissipation rate from 2D-PIV measurements in a vessel stirred by an axial Mixel TTP impeller. Chem. Eng. Sci. 66, 1728–1737.

Fujiwara, A., Minato,D.,Hishida,K.,2004. Effect of bubble diameter on modification of turbulence in an upward pipe flow.Int.J.Heat.Fluid.Fl. 25, 481-488.

Gore, R. A., Crowe, C. T., 1989. Effect of particle size on modulating turbulent intensity.Int. J. Multiph. Flow 15, 279–285.

Gabriele, A., Nienow, A.W., Simmons, M.J.H., 2009. Use of angle resolved PIV to estimate local specific energy dissipation rates for up- and down-pumping pitched blade agitators in a stirred tank. Chem. Eng. Sci. 64, 126–143.

Gabriele, A., Tsoligkas, A.N., Kings, I.N., Simmons, M.J.H., 2011. Use of PIV to measure turbulence modulation in a high throughput stirred vessel with the addition of high Stokes number particles for both up- and down-pumping configurations. Chem. Eng. Sci. 66, 5862-5874.

Hinze, J. O.,1959. Turbulence. McGraw-Hill, New York.

Hetsroni, G., 1989. Particles-turbulence interaction. Int. J. Multiph. Flow 15, 735-746.

Hosokawa,S.,Tomiyama,A.,2004. Turbulence modification in gas–liquid and solid–liquid dispersed two-phase pipe flows. Int.J.Heat.Fluid.Fl.25, 489-498.

Hu, B., 2006. Experimental and theoretical investigation of phase inversion in liquid–liquid dispersions. Ph.D. Thesis. University College London, University of London, London.

Hlawitschka, M.W., Bart, H.-J., 2012. Determination of local velocity, energy dissipation and phase fraction with LIF- and PIV-measurement in a Kühni miniplant extraction column. Chem. Eng. Sci. 69, 138–145.

Iskandrani, A., Kojasoy,G.,2001. Local void fraction and velocity field description in horizontal bubbly flow. Nucl.Eng.Des. 204, 117-128.

Jaworski, Z., Dyster, K.N., Nienow, A.W., 2001.The effect of size, location and pumping direction

of pitched blade turbine impellers on flow patterns: LDA measurement and CFD predictions.Chem. Eng. Res. Des. 79, 887–894.
Kolmogorov, A. N., 1941. The local structure of turbulence in incompressible viscous fluid for very large Reynolds numbers. Dokl. Akad. Nauk Sssr 30, 301–305.
Kresta, S.M., Wood, P.E., 1993a. The flow field produced by a pitched blade turbine: Characterization of the turbulence and estimation of the dissipation rate. Chem. Eng. Sci. 48, 1761–1774.
Kresta, S.M., Wood, P. E., 1993b. The mean flow field produced by a pitched blade turbine: changes in the circulation pattern due to off bottom clearance. Can. J.Chem. Eng. 71, 42–53.
Kenning, V.M., Crowe, C.T., 1997. On the effect of particles on carrier phase turbulence in gas-particle flow. Int.J.Multiph.Flow. 23, 403-408.
Kresta, S., 1998. Turbulence in stirred tanks: Anisotropic, approximate, and applied. Can. J. Chem. Eng. 76, 563–576.
Khan, F.R., 2005. Investigation of turbulent flows and instabilities in a stirred vessel using particle image velocimetry. Ph.D. Thesis, Loughborough University, Loughborough.
Kumara, W. A. S., Elseth, G., Halvorsen, B.M., Melaaen, M.C., 2010. Comparison of Particle Image Velocimetry and Laser Doppler Anemometry measurement methods applied to the oil-water flow in horizontal pipe. Flow Meas. Instrum. 21, 105–117.
Laufhuette, H.D., Mersmann, A., 1985. Local energy dissipation in turbulent stirring of fluids and its significance for the design of stirring equipment. Chem.Ing.Tech. 57, 1104-1105.
Liu, L., 2005. Optical and Computational Studies of Liquid–Liquid Flows. Ph.D.Thesis. Imperial College London, London.
Li, Z., Bao, Y., Gao, Z., 2011. PIV experiments and large eddy simulations of single-loop flow fields in Rushton turbine stirred tanks. Chem. Eng. Sci. 66, 1219–1231.
Maaß, S., Metz, F., Rehm, T., Kraume, M., 2010. Prediction of drop sizes for liquid–liquid systems in stirred slim reactors—Part I:Single stage impellers. Chem.Eng. J. 162,792–801.
Maaß, S., Kraume, M., 2012. Determination of breakage rates using single drop experiments. Chem. Eng. Sci. 70, 146–164.
Morgan, R.G., Markides, C.N., Hale, C.P., Hewitt, G.F., 2012. Horizontal liquid-liquid flow characteristics at low superficial velocities using laser-induced fluorescence. Int. J. Multiph. Flow. 43, 101–117.
Morgan, R.G., Markides, C.N., Zadrazil, I., Hewitt, G.F., 2013. Characteristics of horizontal liquid-liquid flows in a circular pipe using simultaneous high-speed laser-induced fluorescence and particle velocimetry. Int.J.Multiph.Flow.49, 99-118.
Piirto, M., Eloranta, H., Saarenrinne, P., 2000. Interactive software for turbulence analysis from PIV data. In: Proceeding of the 10th International Symposium on Applications of Laser Techniques to Fluid Mechanics. Lisbon, Portugal, July 10-23.
Podgórska, W., 2009. Drop sized distributions in stirred tanks equipped with radial and axial flow impellers. Chem.Proc.Eng. 30, 181-197.
Smagorinsky, J., 1963. General circulation experiments with the primitive equations I. The basic experiment. Mon. Weather Rev. 91, 99-164.
Sharp, K., Kim, K., Adrian, R.,1998. Dissipation estimation around a Rushton turbine using particle image velocimetry. In: Proceedings of the 9th International Symposium on Applied Laser Techniques to Fluid Mechanics.

699 Sheng, J., Meng, H., Fox, R.O., 2000. A large eddy PIV method for turbulence dissipation rate
700 estimation. Chem. Eng. Sci. 55, 4423-4434.
701 Saarenrinne, P., Piirto, M., Eloranta, H., 2001. Experiences of turbulence measurement with PIV.
702 Meas. Sci. Technol. 12, 1904-1910.
703 Sharp, K. V., Adrian, R.J., 2001. PIV Study of small-scale flow structure around a Rushton
704 turbine. AIChE J. 47, 766-778.
705 Sun, X., Paranjape, S., Kim, S., Ozar, B., Ishii, M., 2004. Liquid velocity in upward and downward
706 air-water flows. Ann. Nucl. Energy 31, 357-373.
707 Svensson, F.J.E., Rasmuson, A., 2006. PIV measurements in a liquid–liquid system at volume
708 percentages up to 10% dispersed phase. Exp Fluids.41, 917-931.
709 Sathe, M.J., Thaker, I.H., Strand, T.E., Joshi, J.B., 2010. Advanced PIV/LIF and shadowgraphy
710 system to visualize flow structure in two-phase bubbly flows. Chem. Eng. Sci. 65, 2431-2442.
711 Tsouris, C., Tavlarides, L., 1994. Breakage and coalescence models for drops in turbulent
712 dispersions. AIChE J. 40, 395-406.
713 Tabib, M.V., Schwarz, M.P., 2011. Quantifying sub-grid scale (SGS) turbulent dispersion force
714 and its effect using one-equation SGS large eddy simulation (LES) model in a gas–liquid and
715 a liquid–liquid system. Chem. Eng. Sci. 66, 3071-3086.
716 Tabib, M. V., Lane, G., Yang, W., Schwarz, M.P., 2012. CFD study of single phase and multiphase
717 (liquid-liquid) pump-mixer: Analyzing design parameters, flow structures and turbulence.
718 Chem. Eng. Sci. 80, 55-69.
719 Unadkat, H., Rielly, C.D., Hargrave, G.K., Nagy, Z.K., 2009. Application of fluorescent PIV and
720 digital image analysis to measure turbulence properties of solid-liquid stirred suspensions.
721 Chem. Eng. Res. Des. 87, 573-586.
722 Wu, H., Patterson, G.K., 1989. Laser-Doppler measurements of turbulent-flow parameters in a
723 stirred mixer. Chem. Eng. Sci. 44, 2207-2221.
724 Westerweel, J., Elsinga, G.E., Adrian, R.J., 2013. Particle Image Velocimetry for Complex and
725 Turbulent Flows. Annu. Rev. Fluid Mech. 45, 409-436.
726 Wang, W., Cheng, W., Duan, J., Gong, J., Hu, B., Angeli, P., 2014. Effect of dispersed holdup on
727 drop size distribution in oil-water dispersions: Experimental observations and population
728 balance modeling. Chem. Eng. Sci. 105, 22-31.
729 Zhou, G., Kresta, S.M., 1996. Impact of tank geometry on the maximum turbulence energy
730 dissipation rate for impellers. AIChE J. 42, 2476-2490.
731

732

Nomenclature

A	Empirical constant in Eq.(21)
C_s	Smagorinsky constant
D	Impeller diameter, m
f_e	Correction factor in Eq.(14)
H	Tank height, m
H_{ul}, H_{ll}	Upper and lower limit in Y axils
IA	Interrogation area, m^2
k	Turbulent kinetic energy at each grid, $m^2\ s^{-2}$
$\bar{k}$	Mean turbulent kinetic energy at each grid, $m^2\ s^{-2}$
$\bar{\bar{k}}$	Mean turbulent kinetic energy at fixed region, $m^2\ s^{-2}$
$\bar{\bar{k}}_{16}$, $\bar{\bar{k}}_{32}$	Mean turbulent kinetic energy at fixed region estimated with 16×16 pixels^2 and 32×32 pixels^2, respectively, $m^2\ s^{-2}$
L	Integral length scale, m
N	Rotation speed, s^{-1}
P	Power input, W
P_o	Power number
R_{ul}, R_{ll}	Upper and lower limit in X axils
Re	Reynolds number
s'_{ij}	Strain rate tensors in Eq.(17)
T	Tank diameter, m
U	Instantaneous velocity, m s^{-1}
$\bar{u}$	Time mean velocity, m s^{-1}
u'	Time fluctuating components of the velocity, m s^{-1}
$\bar{\bar{u}}$, $\bar{\bar{v}}$, $\bar{\bar{w}}$	Root mean square of the fluctuating velocity, m s^{-1}
u_p	Periodic velocity component of the angle-resolved velocity, m s^{-1}
u''	Fluctuating components of the angle-resolved velocity, m s^{-1}
V	Volume of the fluid in Eq.(13), m^3
V_k	Coefficient of variation of turbulent kinetic energy in Eq.(25)
V_ε	Coefficient of variation of energy dissipation rate in Eq.(27)
x, y, z	Axial coordinates
Greek letters	
α	Constant
$\Gamma_{i,j}$	General variable at each grid in Eq.(24)
$\bar{\Gamma}$	Mean values of general variable at each grid in Eq.(24)

Δ	Side length of interrogation window, m
Δ_k	Increment degree of turbulent kinetic energy
Δ_ε	Increment degree of energy dissipation rate
ε	Energy dissipation rate at each grid, $m^2\ s^{-3}$
$\bar{\varepsilon}$	Mean energy dissipation rate at each grid, $m^2\ s^{-3}$
$\overline{\varepsilon_T}$	Mean energy dissipation rate in Eq.(13), $m^2\ s^{-3}$
$\bar{\bar{\varepsilon}}$	Mean energy dissipation rate at fixed region, $m^2\ s^{-3}$
$\bar{\bar{\varepsilon}}_{16}$, $\bar{\bar{\varepsilon}}_{32}$	Mean energy dissipation rate at fixed region, estimated with 16×16 pixels^2 and 32×32 pixels^2, respectively, $m^2\ s^{-3}$
η	Modified Kolmogorov length in Eq.(15), m
θ	Resolved angle
λ_k	Kolmogorov length scale, m
μ	Dynamic viscosity, $N\ s\ m^{-2}$
ν	Kinematic viscosity, $m^2\ s^{-1}$
ρ	Density, $kg\ m^{-3}$
σ_k	Standard deviation of turbulent kinetic energy in Eq.(25)
σ_ε	Standard deviation of energy dissipation rate in Eq.(27)
ϕ	Dispersed volume fraction
τ_{ij}	SGS stress tensor
ψ_i	General variable in Eq.(23)
$\bar{\psi}$	Mean value of general variable in Eq.(23)

Subscripts

c	Continuous phase
d	Dispersed phase
DA	By dimensional analysis
DE	By direct evaluation
i, j	Tensor indices
m	Mixing phase
MDE	By modified direct evaluation
RMS	Root mean square
SGS	Using Smagorinsky sub-grid scale

Abbreviations

PIV	Particle image velocimetry
TKE	Turbulent kinetic energy
EDR	Energy dissipation rate

734

735

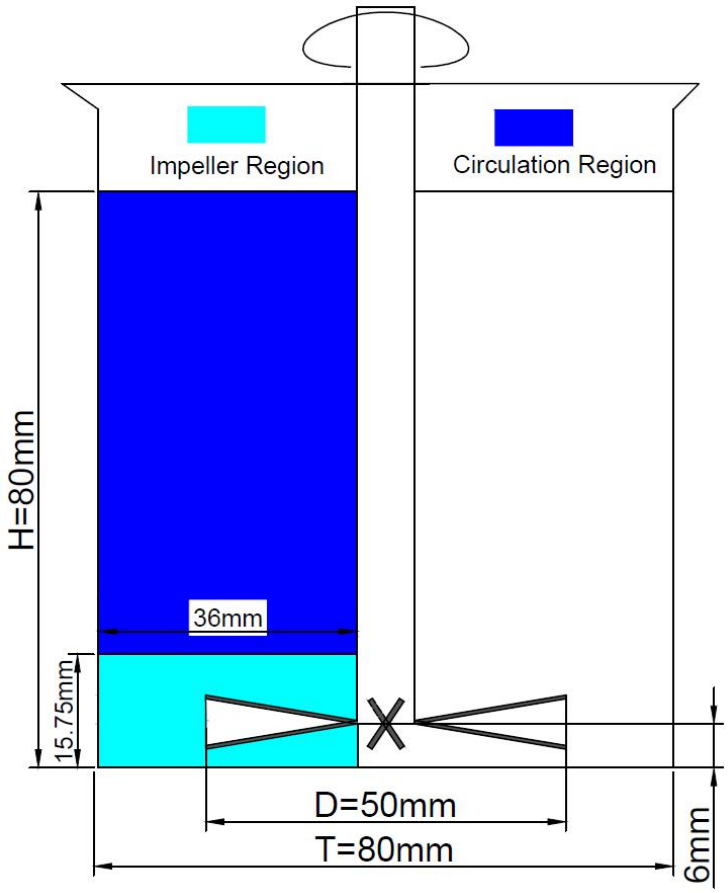

(a)

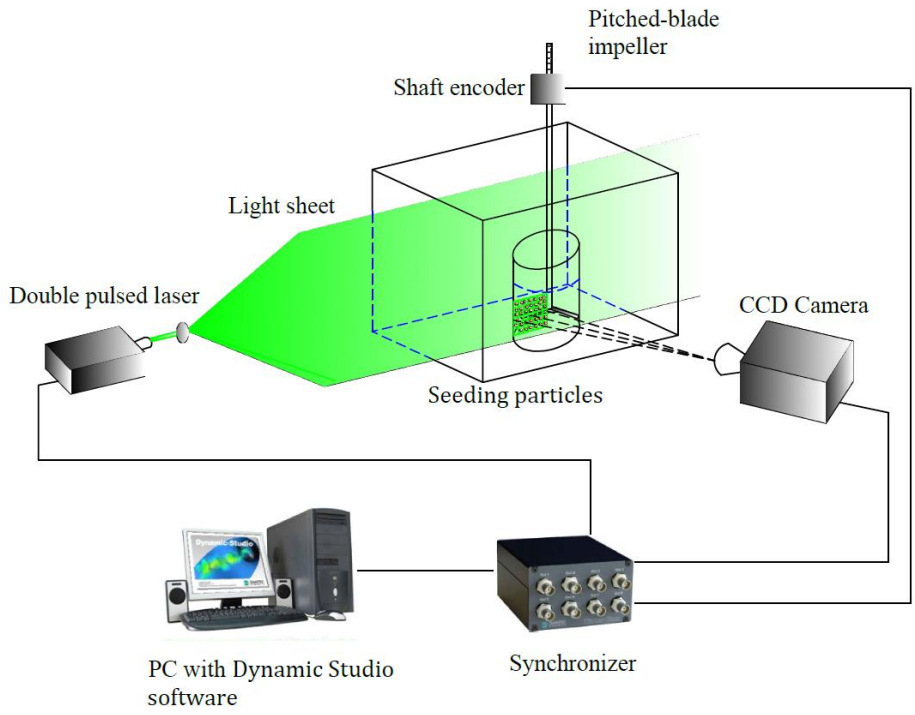

(b)

Fig. 1 Schematic map of experiments system :(a) stirred tank geometry; (b) PIV measuring method.

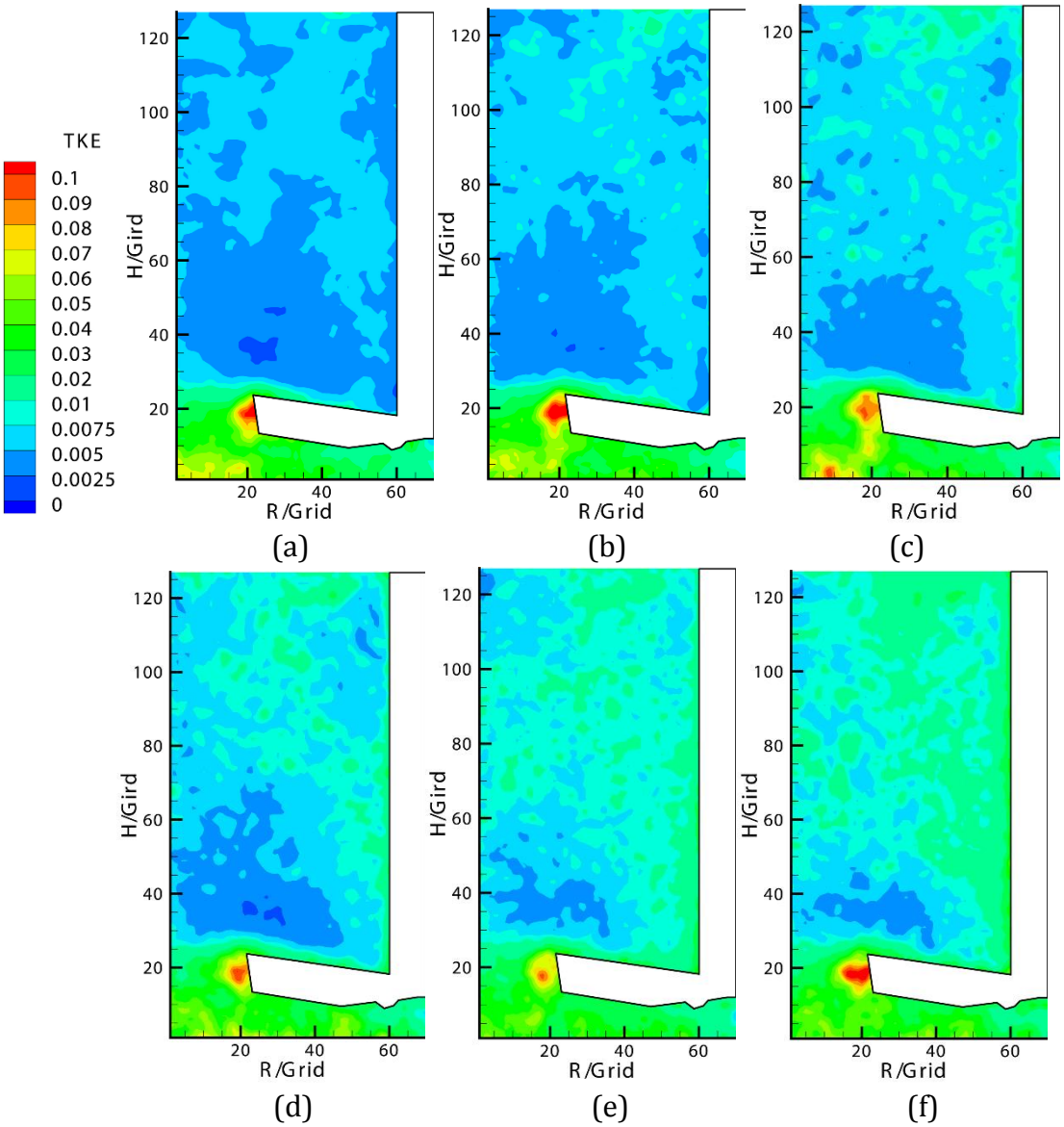

Fig. 2 Angle-resolved TKE distribution of 0° at different dispersion fractions with 32×32 pixels^2: (a) 0% (pure oil phase); (b) 0.2%; (c) 0.5%; (d) 0.7%; (e) 1.0%; (f) 1.3%.

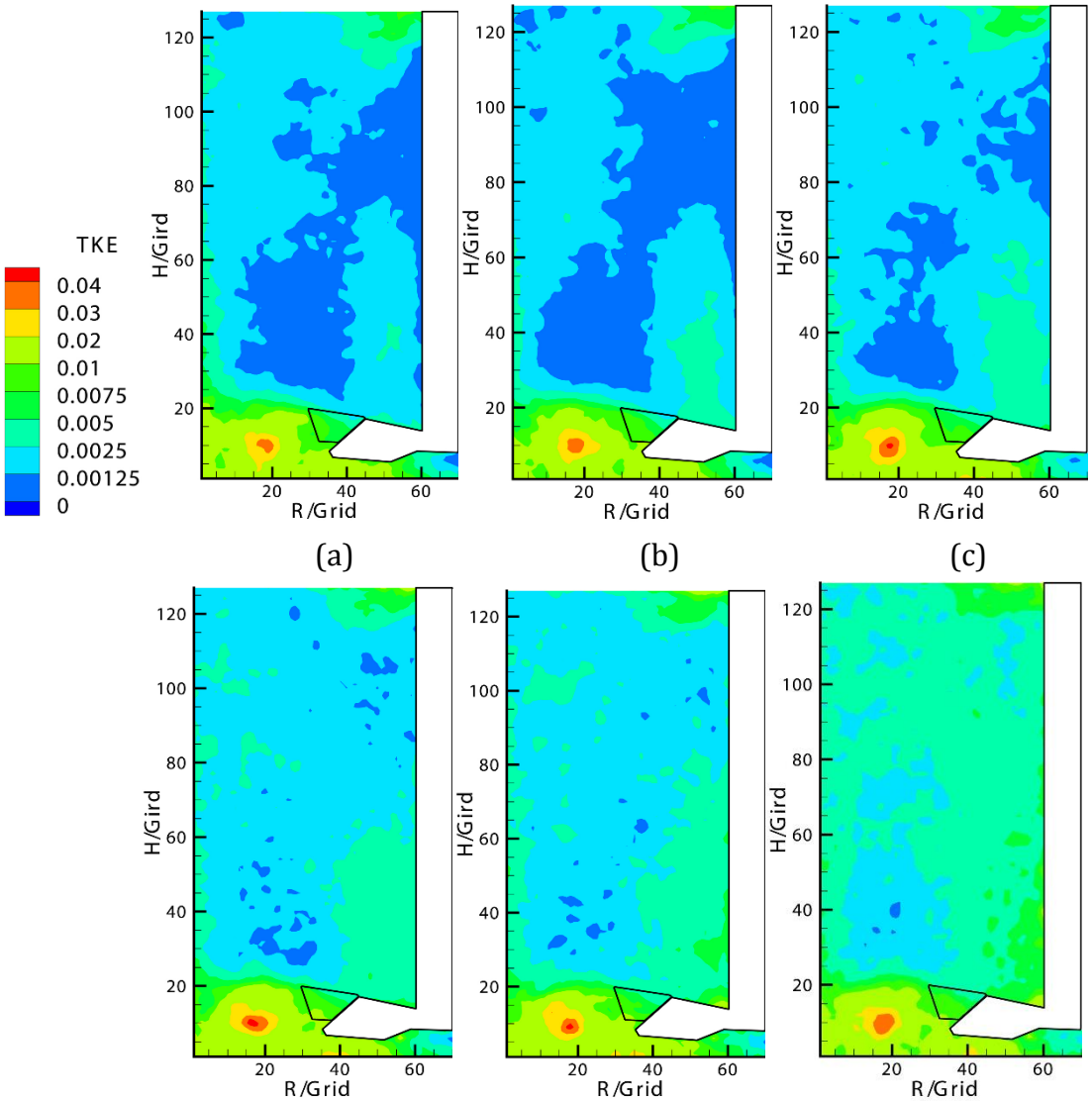

Fig. 3 Angle-resolved TKE distribution of 45° at different dispersion fractions with 32×32 pixels^2: (a) 0% (pure oil phase); (b) 0.2%; (c) 0.5%; (d) 0.7%; (e) 1.0%; (f) 1.3%.

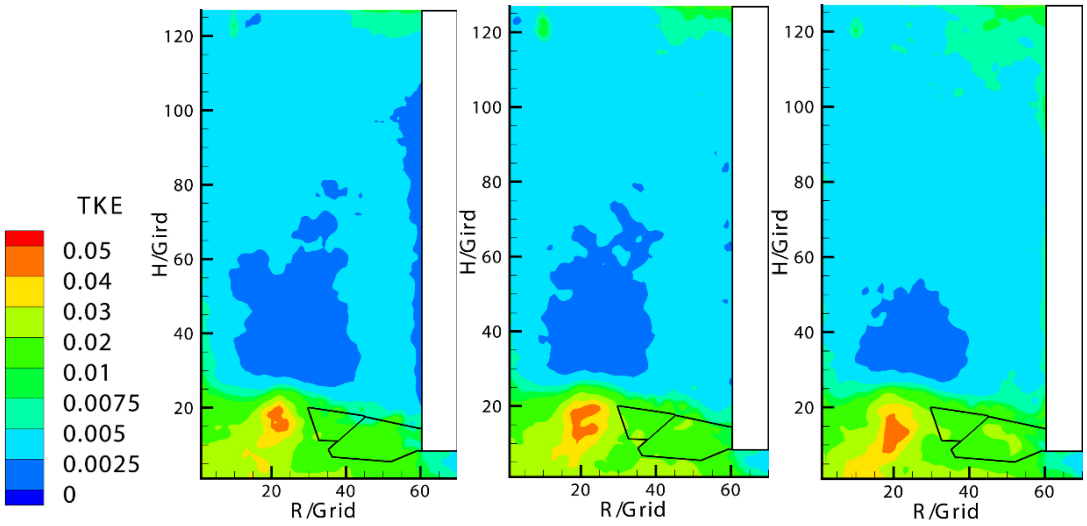

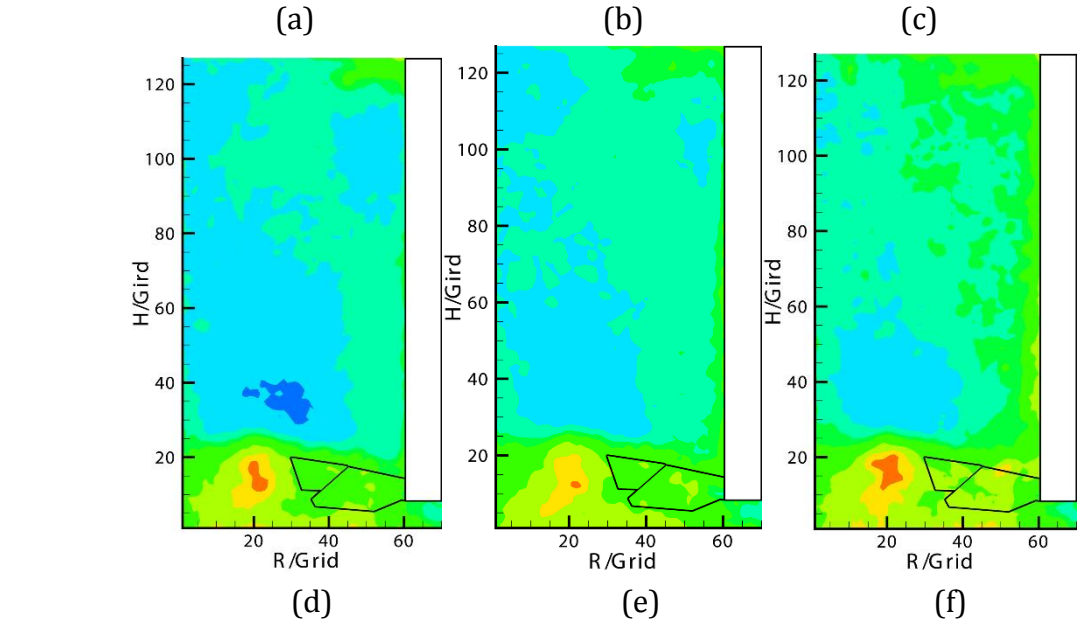

Fig. 4 Mean TKE distribution at different dispersion fractions with 32×32 pixels²: (a) 0% (pure oil phase); (b) 0.2%; (c) 0.5%; (d) 0.7%; (e) 1.0%; (f) 1.3%.

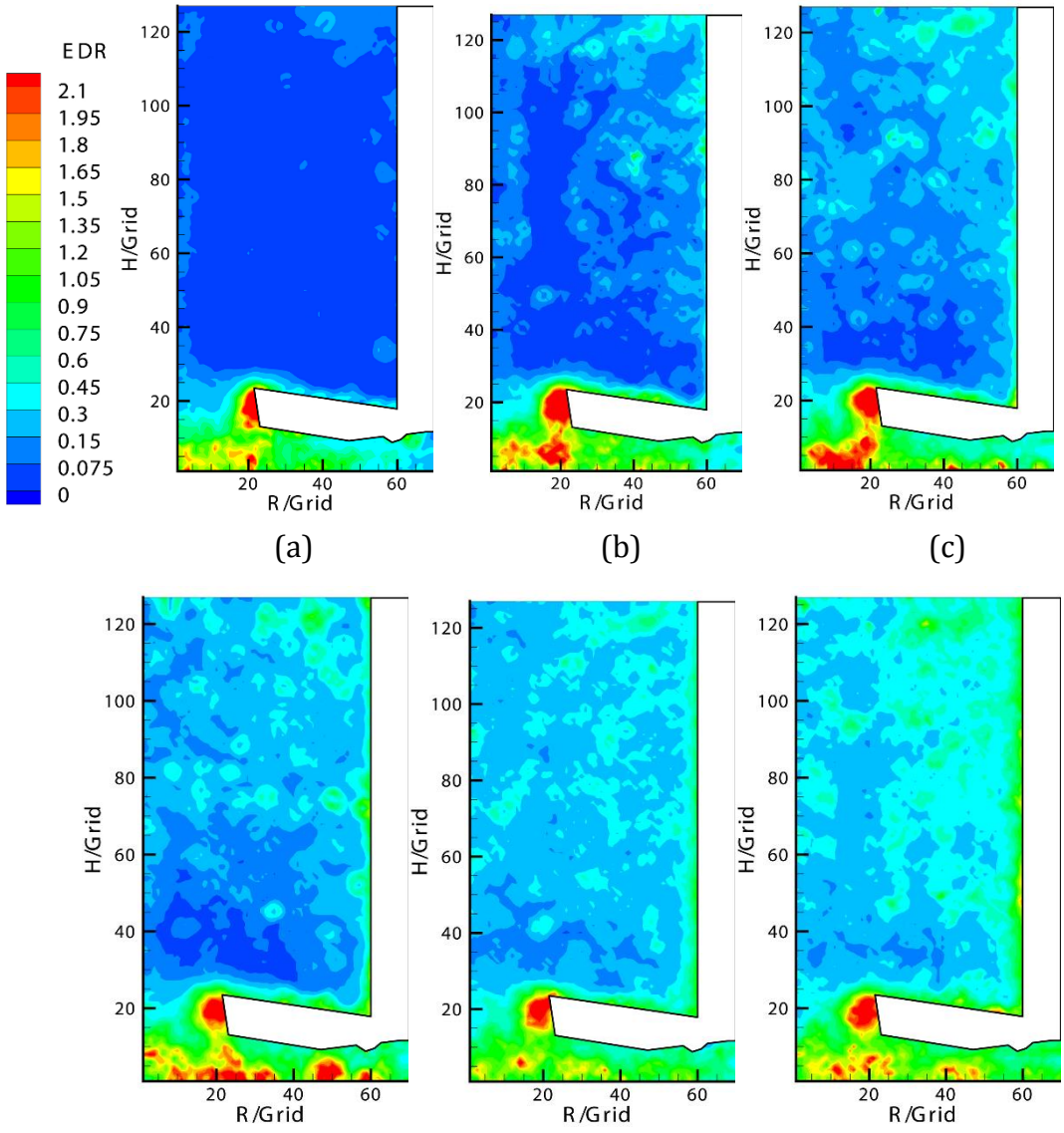

(d) (e) (f)

Fig. 5 Angle-resolved EDR distribution of 0°at different dispersion fractions with 32×32 pixels²: (a) 0% (pure oil phase); (b) 0.2%; (c) 0.5%; (d) 0.7%; (e) 1.0%; (f) 1.3%.

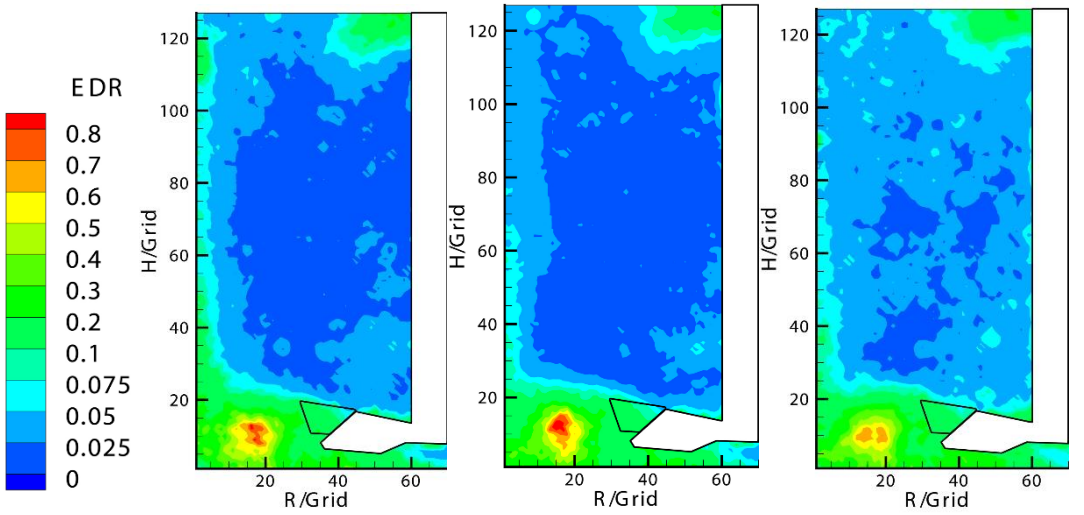

(a) (b) (c)

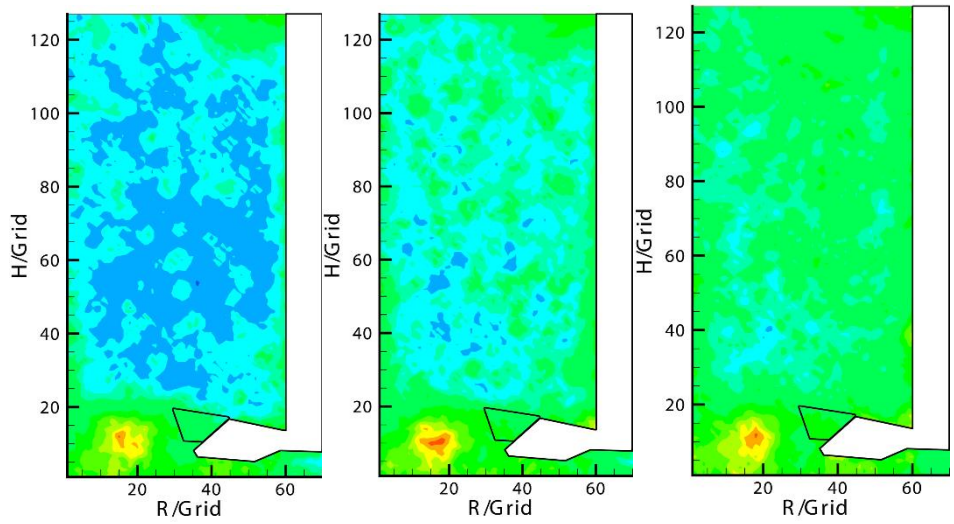

(d) (e) (f)

Fig. 6 Angle-resolved EDR distribution of 45°at different dispersion fractions with 32×32 pixels²: (a) 0% (pure oil phase); (b) 0.2%; (c) 0.5%; (d) 0.7%; (e) 1.0%; (f) 1.3%.

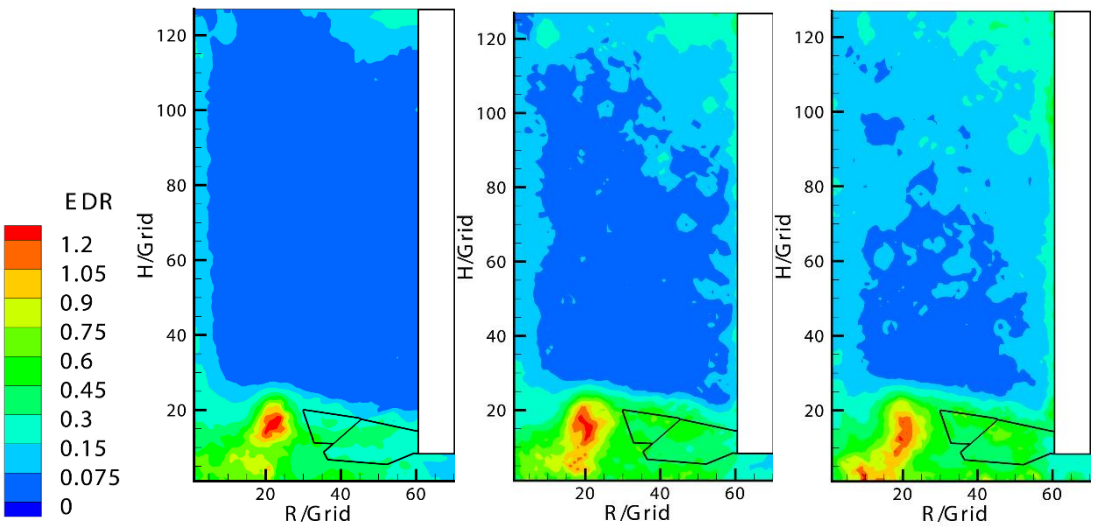

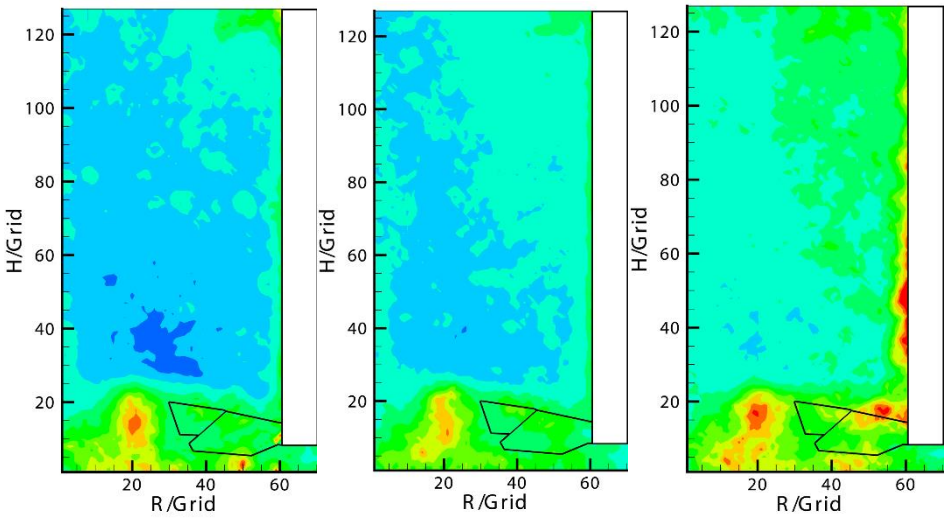

Fig. 7 Angle-resolved mean EDR distribution at different dispersion fractions with 32×32 pixels²: (a) 0% (pure oil phase); (b) 0.2%; (c) 0.5%; (d) 0.7%; (e) 1.0%; (f) 1.3%.

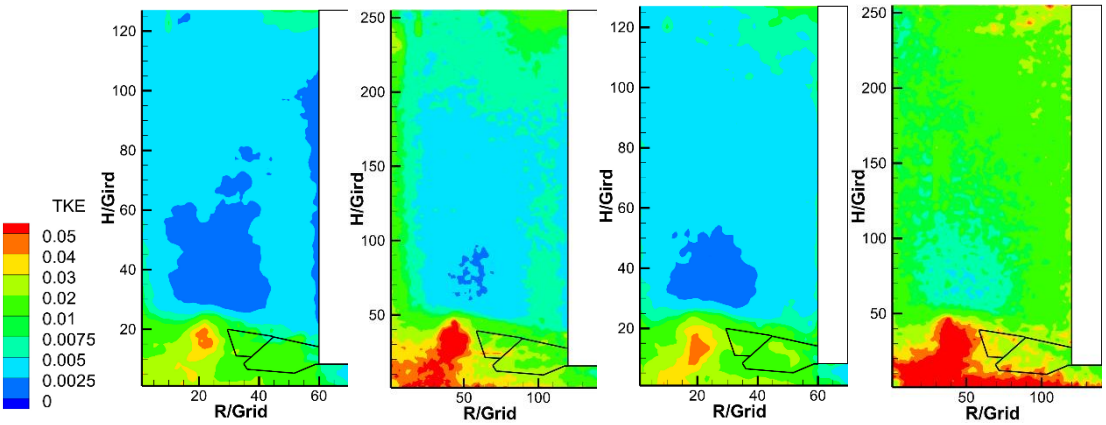

32×32 pixels² 16×16 pixels² 32×32 pixels² 16×16 pixels²

(a) pure oil phase (b) 0.5% dispersed system

Fig. 8 Comparison of mean TKE distribution between different spatial resolutions

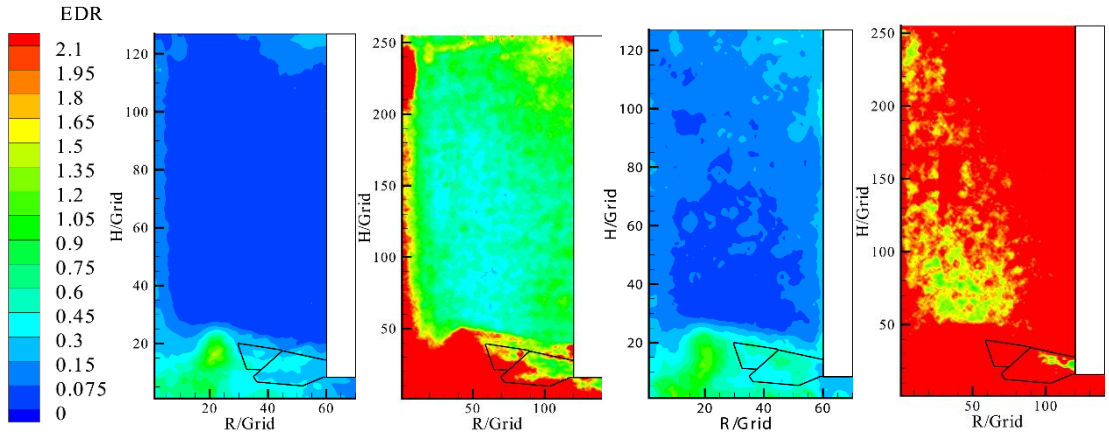

32×32 pixels² 16×16 pixels² 32×32 pixels² 16×16 pixels²

(a) pure oil phase (b) 0.5% dispersed system

Fig. 9 Comparison of mean EDR distribution between different spatial resolutions with DE method.

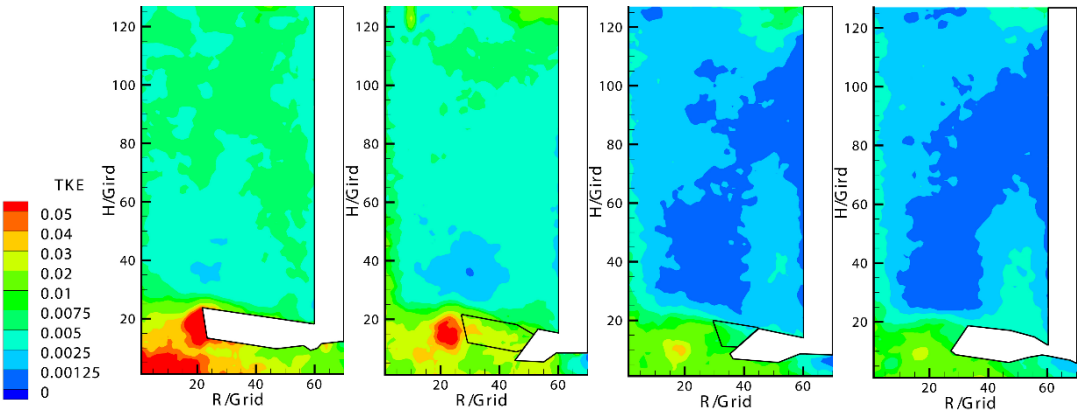

(a) 0° (b) 22.5° (c) 45° (d) 67.5°

Fig. 10 Angle-resolved TKE distribution at different angles relative to the impeller blade in pure oil phase (32×32 pixels²).

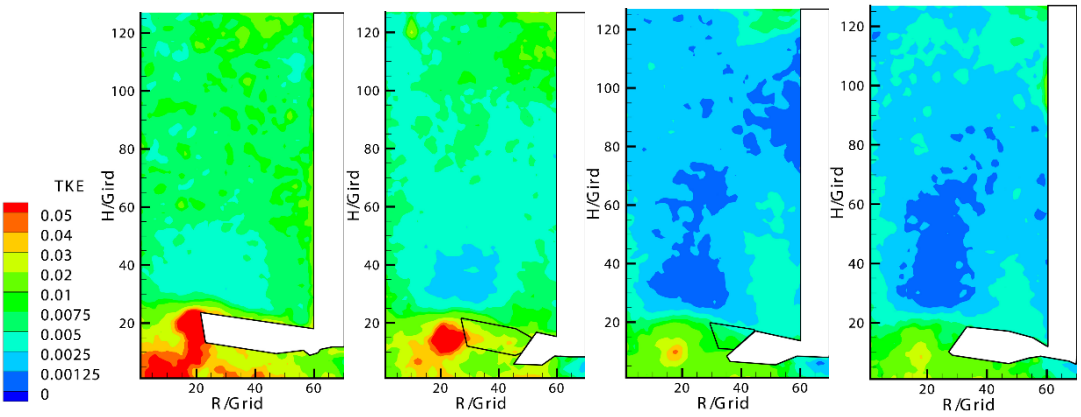

(a) 0° (b) 22.5° (c) 45° (d) 67.5°

Fig. 11 Angle-resolved TKE distribution at different angles relative to the impeller blade in 0.5% dispersion (32×32 pixels²).

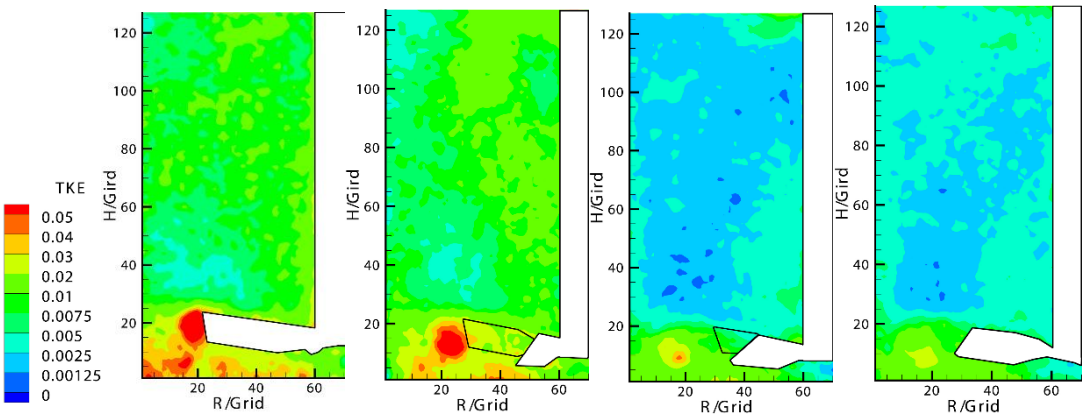

(a) 0° (b) 22.5° (c) 45° (d) 67.5°

Fig. 12 Angle-resolved TKE distribution at different angles relative to the impeller blade in 1.0% dispersion (32×32 pixels²).

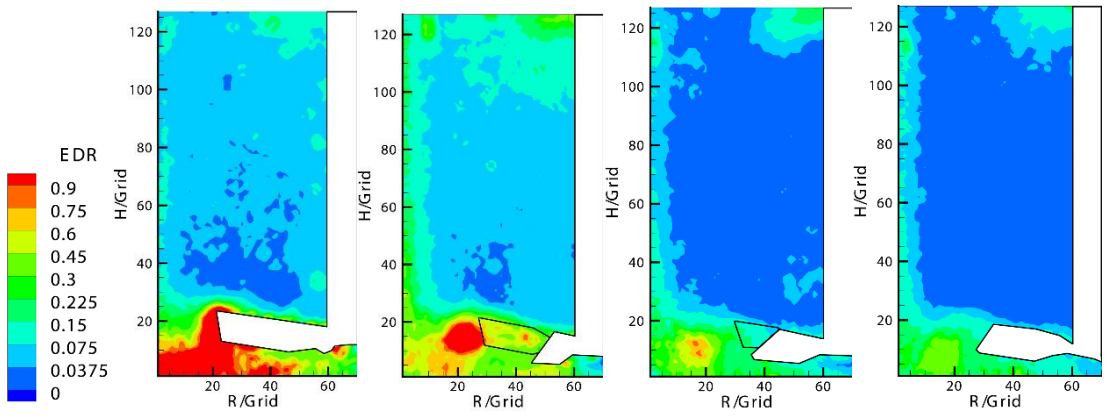

(a) 0° (b) 22.5° (c) 45° (d) 67.5°

Fig. 13 Angle-resolved EDR estimated by DE method at different angles relative to the impeller blade in pure oil phase (32×32 pixels²).

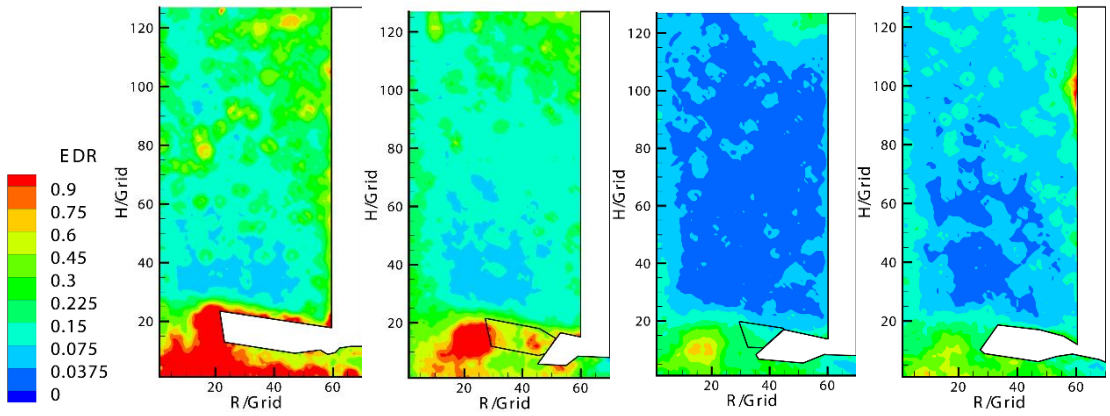

(a) 0° (b) 22.5° (c) 45° (d) 67.5°

Fig. 14 Angle-resolved EDR estimated by DE method at different angles relative

to the impeller blade in 0.5% dispersion (32×32 pixels^2).

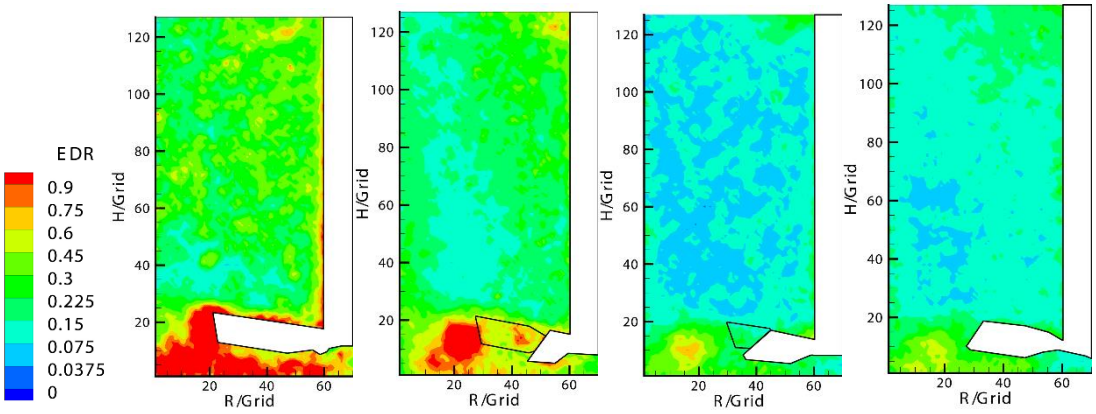

(a) 0° (b) 22.5° (c) 45° (d) 67.5°

Fig. 15 Angle-resolved EDR estimated by DE method at different angles relative to the impeller blade in 1.0% dispersion (32×32 pixels^2).

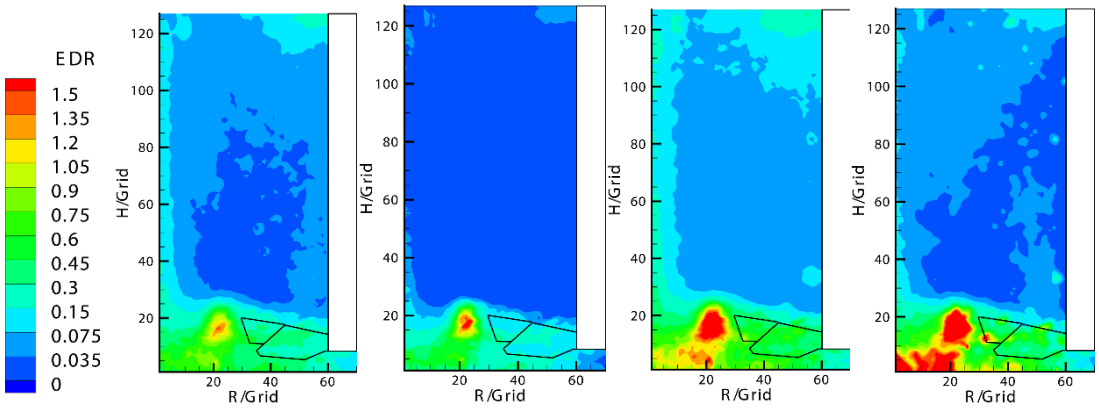

(a) (b) (c) (d)

Fig. 16 Comparison of mean EDR of single oil phase using different estimation methods with 32×32 pixels^2: (a) DE; (b) LES; (c) MDE; (d) DA.

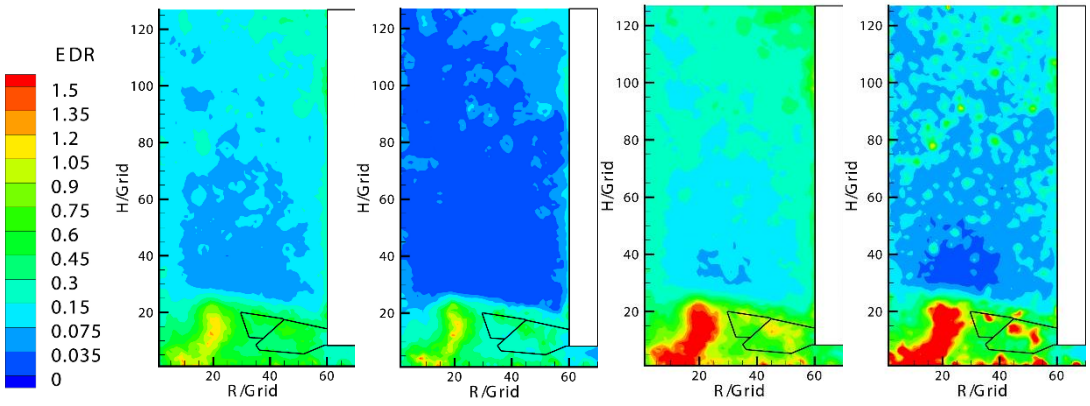

(a) (b) (c) (d)

Fig. 17 Comparison of mean EDR of 0.5% dispersed system using different estimation methods with 32×32 pixels^2 : (a) DE; (b) LES; (c) MDE; (d) DA.

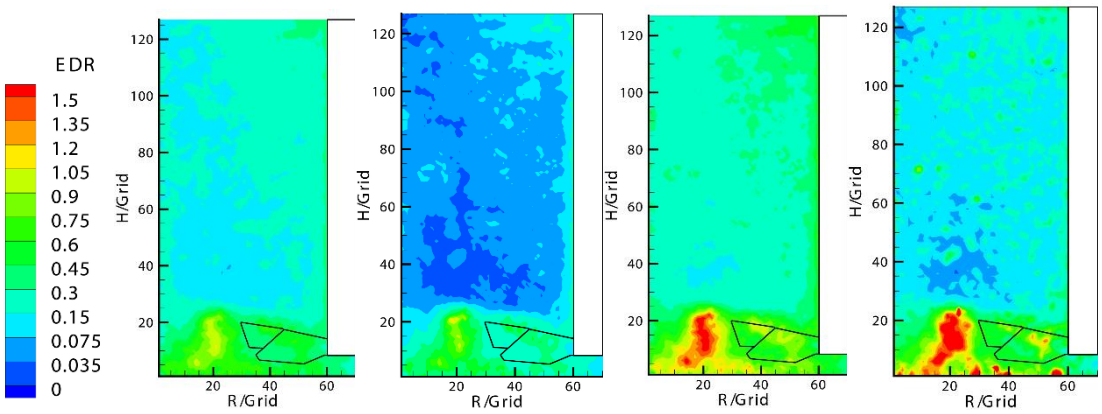

Fig. 18 Comparison of mean EDR of 1.0% dispersed system using different estimation methods with 32×32 pixels^2 : (a) DE; (b) LES; (c) MDE; (d) DA.

Table.1 Physical properties of experimental fluids

	Exxsol D130	Glycerol solution 80 wt.% in 20% water
Density (kgm^{-3})	824	1205
Viscosity (mPa·s)	5.0	47
Refractive index	1.45	1.45

Table.2 Angle averaged mean TKE values of different dispersion at impeller region, circulation region and full region.

TKE($m^2 s^{-2}$)	Impeller region	Circulation region	Full region
pure	0.0178	0.0031	0.0054
0.2%	0.0198(**1.11** times to pure)	0.0034(**1.10**)	0.0060(1.11)
0.5%	0.0199(**1.11**)	0.0039(1.26)	0.0064(1.19)
0.7%	0.0197(**1.11**)	0.0050(1.61)	0.0073(1.35)
1.0%	0.0191(**1.07**)	0.0056(1.81)	0.0078(1.44)
1.3%	0.0223(**1.25**)	0.0071(**2.29**)	0.0095(**1.76**)
Average(0.2-1.3%)	0.0202(**1.13**)	0.0050(**1.61**)	0.0074(**1.37**)

E.G. (1.11 times to pure) indicates the mean TKE of 0.2% dispersion divided by the mean TKE of pure system

Table.3 Angle averaged mean EDR values of different dispersions at impeller region, circulation region and full region.

EDR($m^2 s^{-3}$)	Impeller region	Circulation region	Full region
pure	0.4198	0.0517	0.1096
0.2%	0.5144(1.23 times to pure)	0.0812(1.57)	0.1493(1.36)
0.5%	0.5213(1.24)	0.1082(2.09)	0.1731(1.58)
0.7%	0.5313(1.27)	0.1434(2.77)	0.2044(1.86)
1.0%	0.508(1.21)	0.1721(3.33)	0.2249(2.05)
1.3%	0.6609(1.57)	0.3107(6.01)	0.3658(3.34)
Average(0.2-1.3%)	0.5472(**1.30**)	0.1631(**3.15**)	0.2235(**2.04**)

Table.4 Angle averaged mean TKE values estimated from different spatial resolutions at full region.

TKE ($m^2 s^{-2}$)	32×32 $pixels^2$	16×16 $pixels^2$	increment Δ_k
pure	0.0054	0.0098	**81%**
0.5%	0.0064	0.0171	**166%**
1%	0.0078	0.0271	**249%**

Table.5 Angle averaged mean EDR values with DE method estimated from different spatial resolutions at full region.

EDR ($m^2 s^{-3}$)	32×32 $pixels^2$	16×16 $pixels^2$	increment Δ_ε

pure	0.1096	1.2878	**1075%**
0.5%	0.1731	3.2773	**1793%**
1%	0.2249	5.6432	**2409%**

Table.6 Angle averaged mean TKE values of full region at different measuring angles.

TKE($m^2 s^{-2}$)	pure	0.2%	0.5%	0.7%	1.0%	1.3%
Angle1	0.0094	0.0109	0.0113	0.0116	0.0124	0.0143
Angle2	0.0068	0.0079	0.0079	0.0109	0.0110	0.0142
Angle3	0.0029	0.0028	0.0032	0.0035	0.0037	0.0045
Angle4	0.0026	0.0025	0.0033	0.0033	0.0040	0.0050
Average	0.0054	0.0060	0.0064	0.0073	0.0078	0.0095
Standard deviation	0.0028	0.0035	0.0034	0.0039	0.0039	0.0047
Coefficient of Variation	52%	58%	53%	54%	51%	50%

Table.7 Angle averaged mean EDR values at full region with different measuring angles

EDR($m^2 s^{-3}$)	pure	0.2%	0.5%	0.7%	1.0%	1.3%
Angle1	0.1766	0.2823	0.3301	0.3693	0.3909	0.4917
Angle2	0.1464	0.2079	0.2035	0.2620	0.2571	0.6296
Angle3	0.0629	0.0550	0.0654	0.0851	0.1134	0.1465
Angle4	0.0525	0.0519	0.0934	0.1012	0.1382	0.1952
Average	0.1096	0.1493	0.1731	0.2044	0.2249	0.3658
Standard deviation	0.0531	0.0994	0.1043	0.1177	0.1101	0.2016
Coefficient of Variation	48%	67%	60%	58%	49%	55%

Table.8 Angle averaged mean EDR values with different methods at full region.

EDR($m^2 s^{-3}$)	DE	LES(times to DE)	MDE(times to DE)	DA(times to DE)
pure	0.1096	0.0531(0.48)	0.1752(1.60)	0.1606(1.47)
0.2%	0.1493	0.0790(0.53)	0.2478(1.66)	0.2239(1.50)
0.5%	0.1731	0.0873(0.50)	0.3064(1.77)	0.2499(1.44)
0.7%	0.2044	0.1034(0.50)	0.3561(1.74)	0.3038(1.49)
1.0%	0.2249	0.1033(0.46)	0.3536(1.57)	0.2436(1.08)
1.3%	0.3658	0.2126(0.58)	0.6442(1.76)	0.4551(1.24)
Average times	1.00	**0.51**	**1.68**	**1.37**

Table.9 Angle averaged mean EDR values with different methods at impeller region.

EDR($m^2 s^{-3}$)	DE	LES(times to DE)	MDE(times to DE)	DA(times to DE)
pure	0.4198	0.2819(0.67)	0.6824(1.63)	0.7854(1.87)
0.2%	0.5144	0.3799(0.74)	0.8615(1.67)	1.0102(1.96)
0.5%	0.5213	0.3754(0.72)	0.9188(1.76)	1.0623(2.04)

0.7%	0.5313	0.3821(0.72)	0.9449(1.78)	1.1573(2.18)
1.0%	0.5080	0.3299(0.65)	0.8082(1.59)	0.7820(1.54)
1.3%	0.6609	0.4832(0.73)	1.1562(1.75)	1.1366(1.72)
Average times	1.00	**0.71**	1.70	**1.89**

869

870 Table.10 Angle averaged mean EDR values with different methods at circulation
871 region.

EDR ($m^2 s^{-3}$)	DE	LES(times to DE)	MDE(times to DE)	DA(times to DE)
pure	0.0517	0.0104(0.20)	0.0805(1.56)	0.0441(0.85)
0.2%	0.0812	0.0229(0.28)	0.1334(1.62)	0.0772(0.95)
0.5%	0.1082	0.0336(0.31)	0.1921(1.77)	0.0984(0.91)
0.7%	0.1434	0.0514(0.36)	0.2463(1.72)	0.1446(1.00)
1.0%	0.1721	0.0610(0.35)	0.2688(1.56)	0.1432(0.83)
1.3%	0.3107	0.1621(0.52)	0.5487(1.77)	0.3280(1.06)
Average times	1.00	0.34	1.67	**0.93**

872